Computational Materials Science 240 (2024) 113002

Contents lists available at ScienceDirect

Computational Materials Science

journal homepage: www.elsevier.com/locate/commatsci

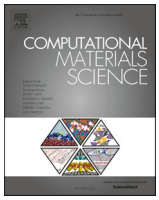

Full Length Article

Effects of element type on accuracy of microstructural mesh crystal plasticity finite element simulations and comparisons with elasto-viscoplastic fast Fourier transform predictions

Jacob Weiss, Marko Knezevic *

Department of Mechanical Engineering, University of New Hampshire, Durham, NH 03824, USA

ARTICLE INFO

Keywords:
Micromechanics
Crystal Plasticity
Finite element methods
CPFE
EVPFFT

ABSTRACT

In this work, we performed massive crystal plasticity finite element (CPFE) simulations to reveal the effects of element type on the accuracy of predicted mechanical fields and overall response over explicit periodic grain structure meshes of polycrystalline Cu during simple tension (ST), simple shear (SS), and a strain path change from ST to SS. Post-processing of the results provided a list of guidance for effective CPFE modeling of explicit microstructures. First, it was confirmed that quadratic tetrahedral elements (C3D10) are the most suitable for CPFE modeling owing to their accuracy, efficiency, and flexibility to describe complex geometries intrinsic to microstructures. Moreover, these elements predicted the overall response between the stiff linear hexahedral (C3D8) and compliant quadratic hexahedral (C3D20) elements. Next, quadratic hexahedral elements with reduced integration (C3D20R) arose as the second choice for CPFE modeling owing to their accuracy and computational efficiency but these elements generally require more memory than C3D10 elements. These elements were also effective in relaxing the issue of volumetric locking intrinsic to C3D20 elements. The issue could not be eliminated by involving C3D20H or C3D20RH hybrid elements with constant pressure. Finally, corresponding simulations of the same explicit grain structure represented in voxel-based formats using elasto-viscoplastic fast Fourier transform (EVPFFT) full-field verified the overall response but predicted the local fields to deviate with plastic strain for all element types.

1. Introduction

Modeling of polycrystalline metals increasingly employs spatio-temporal microstructures allowing constituent grains to interact explicitly with each other while ensuring the state of strain compatibility and arriving at the stress equilibrium [1–6]. Such modeling is termed the full-field approach to modeling polycrystalline microstructures of metals. Purposely, the full-field modeling of microstructures accounts for the topological structure of constituent grains and their evolution while calculating the micromechanical fields and therefore facilitates relatively accurate predictions and understanding of complex phenomena pertaining to the material behavior. The plasticity fields modeling at the grain scale is vital for understanding and predicting mechanical extremes for damage/void nucleation driven by local stress/strain concentrations at weak microstructural regions. The governing equation of stress equilibrium in full-field modeling is usually solved numerically using the finite element method (FEM) over a finite element mesh [2,7,8] or a Green's function method relying on the fast Fourier transform (FFT) algorithm to solve the convolution integral for stress equilibrium over a voxel-based microstructural cell [9]. The former class of models is referred to as the crystal plasticity finite element (CPFE) models [10,11], while the latter is the elasto-visco plastic FFT (EVPFFT) models [12,13]. EVPFFT is a widely used computationally efficient substitute to CPFE for simulating mechanical fields over a microstructural cell/cube and the overall response of polycrystalline grain structures in 3D as average over the cube [14–17]. It avoids many challenges pertaining to mesh generation for CPFE because it utilizes voxel-based microstructures. Both CPFE and EVPFFT involve a single crystal plasticity constitutive law describing the material behavior under boundary conditions in arriving at a solution in terms of a work-conjugated stress–strain measures. The single crystal plasticity constitutive law embedded at every FE material/integration point (CPFE) or voxel

* Corresponding author at: University of New Hampshire, Department of Mechanical Engineering, 33 Academic Way, Kingsbury Hall, W119, Durham, New Hampshire 03824, United States.
E-mail address: marko.knezevic@unh.edu (M. Knezevic).

https://doi.org/10.1016/j.commatsci.2024.113002
Received 28 August 2023; Received in revised form 13 January 2024; Accepted 4 April 2024
Available online 10 April 2024

(EVPFFT) implies that the micromechanical fields and overall response are governed by crystal lattice orientation and crystallographic deformation mechanisms. Moreover, the evolution of inter- and intragranular misorientation fields over grains, grain shapes, and grain boundary character distributions (GBCD) are also captured to influence local/overall response [18,19].

To elucidate heterogeneous mechanical fields, the full-field modeling using CPFE and EVPFFT requires generation of polycrystalline domains [20,21]. A BlueQuartz software package called DREAM.3D (Digital-Representation-Environment-for-Analyzing-Microstructures in 3D) is a sophisticated tool to generate voxel-based synthetic microstructures [22]. Statistics of grain size distribution, grain shape, and orientation and misorientation distributions are inputs into DREAM.3D to generate statistically equivalent voxel-based microstructural cells. Similarly, synthetic voxel-based microstructures can be obtained using the Voronoi tessellation [23–28]. Furthermore, voxel-based synthetic microstructures can be created by microstructure evolution models such as Potts (Monte-Carlo) [29,30], phase-field [31], and cellular automata [32,33] grain growth models. Finally, experimental techniques have been developed to acquire real grain structure data in 3D. These experimental techniques include focused ion beam (FIB) electron backscattered diffraction (EBSD) serial sectioning [34–39]. A similar technique is robotic serial sectioning complemented with EBSD [40,41] Finally, nf HEDM (near-field high-energy X-ray diffraction microscopy) is a very recent technique [42–48]. The data from these techniques is also represented by voxels. Post processing of so acquired experimental data is facilitated by DREAM.3D including the generation of triangular surface mesh over every grain. The surface mesh is a convenient input into volume mesh generation tools [49].

Voxel-based microstructures are a direct input into EVPFFT. In general, a voxel-based grid describing a microstructure of sufficient resolution requires a very large number of voxels to represent complex geometries of grains. If every voxel is considered as a hexahedral finite element [50], the mesh would contain the same number of finite elements as voxels requiring a computational cost beyond practical limits. Moreover, direct meshes from voxels develop artificial field localizations at interfaces and triple junctions due to the so called stair-case instead of smooth/flat grain boundaries unavoidable in such meshes [51,52]. In summary, a microstructure in a voxel-based format is an easy way to initialize CPFE simulations with hexahedral elements but many hexahedral elements equal to the number of voxels makes such simulations computationally demanding and, even more importantly, the stair-stepped grain boundaries intrinsic to such models make the simulations less accurate. Therefore, extra steps to convert the voxels into conformal FE meshes are needed.

Given the surface triangular mesh decorating grains from DREAM.3D, we have developed procedures relying on Patran to mesh volumes of individual grains into tetrahedral elements conforming between grains [49]. The conformal mesh means that the neighboring grains share nodes at grain boundaries. The meshing procedures were advanced to build meshes of polycrystals in various specimen geometries other than cubic microstructural cells [53]. Examples in microforming [54,55] and micro-mechanical testing [26] have been simulated. Several works relied on the procedure to study shear band formation [56] and explicit twins in microstructures [57,58]. Besides tetrahedral meshes, interface conformal meshes of polycrystals consisting of hexahedral elements can be generated from voxel-based geometries using the Sculpt meshing tool [51,59,60], an application of the Cubit Meshing and Geometry Toolkit developed and maintained at SNL (Sandia National Laboratories) [61].

Mesh convergence studies of polycrystalline microstructures have been performed in literature [62,63]. Such studies are more involved compared to conventional FE analyses as they are not only computationally demanding but also require explicit meshing of individual grains involving many elements. Moreover, the mesh convergence is influenced by individual crystal orientations of grains and localized loading conditions. Representative volume element (RVE) studies for polycrystalline microstructures while varying factors such as initial textures, hardening models and boundary conditions have also been performed [62,64–66]. These works provided a list of useful guidelines for effective CPFE modeling.

In this paper, a large number of massive CPFE simulations of explicit microstructures are carried out and postprocessed to investigate the effects of various element types on the accuracy of CPFE simulations in predicting mechanical fields and overall response and efficiency. A parallel computing infrastructure is used because the simulations are computationally demanding and require significant memory size. The work complements a recent study into mesh resolution consisting of either fully integrated linear or quadratic hexahedral (*hex or brick*) and tetrahedral (*tet*) elements [63] by further evaluating the effects of a broader element type library on accuracy, computational efficiency, and memory usage. A wide range of elements in the Abaqus element library provides opportunities to increase accuracy, efficiency, and flexibility in modeling different geometries/structures. An initial voxel-based polycrystalline microstructural cell is created synthetically in DREAM.3D and converted to interface-conformal tet and hex meshes at two levels of discretization. Since boundary conditions may affect the results in addition to grain structure, three types of boundary conditions involving simple tension (ST), simple shear (SS), and a strain path change from ST to SS (ST + SS) are imposed over the models. Simulations of ST, SS, and ST + SS are performed using C3D8, C3D8R, C3D20, C3D20H, C3D20R, C3D20RH, C3D10, C3D10H, and C3D10MH element types. Comparisons of the results in terms of the accuracy of mechanical fields and overall response and computational efficiency and memory are presented and discussed. Even though CPFE is a widely used tool to understand and predict the mechanical response of polycrystalline materials, no systematic study into the element types exists in current literature. The aim is to provide additional guidance for effective CPFE modeling of explicit microstructures. The paper also compares and verifies the CPFE results with the EVPFFT predictions. To this end, the EVPFFT code was advanced to implement an identical hardening law to the one present in CPFE and both codes were calibration using experimental data of polycrystalline copper (Cu) to facilitate fair comparisons. Although a study comparing EVPFFT and CPFE exist in the literature [67], we regard our study as more thorough because of the robust grain structure meshing with variable element types of high resolution.

2. Modeling framework

This section summarizes two crystal plasticity models for completeness of the study. Both models incorporate the same hardening law fit to model the response of polycrystalline Cu.

2.1. CPFE

In the finite strains kinematics of CPFE, the gradient of deformation tensor, $\mathbf{F}$, imposed from Abaqus at every integration point is multiplicatively decomposed into an elastic part, $\mathbf{F}^*$, and a plastic part, $\mathbf{F}^p$, as [68,69]

$$\mathbf{F} = \mathbf{F}^*\mathbf{F}^p \tag{1}$$

While the elastic part embeds elastic stretching and any lattice rotation, the plastic part embeds the plastic deformation by crystallographic slip. A single crystal constitutive law in CPFE is elasto-viscoplastic and relates a pair of work conjugated stress and strain measures as [70,71]

$$\mathbf{T}^* = \mathbf{C}\colon \mathbf{E}^*, \mathbf{T}^* = \mathbf{F}^{*-1}\{(\det\mathbf{F}^*)\boldsymbol{\sigma}\}\mathbf{F}^{*-T}, \mathbf{E}^* = \frac{1}{2}\{\mathbf{F}^{*T}\mathbf{F}^* - \mathbf{I}\} \tag{2}$$

where $\mathbf{C}$ is the elastic stiffness tensor, $\boldsymbol{\sigma}$ is the Cauchy-stress tensor, $\mathbf{T}^*$ is the second Piola–Kirchhoff-stress tensor, and $\mathbf{E}^*$ is the Green-

Lagrangian-strain tensor. The flow rule of $\mathbf{F}^p$ is

$$\dot{\mathbf{F}}^p = \mathbf{L}^p\mathbf{F}^p, \mathbf{L}^p = \sum_s \dot{\gamma}^s \mathbf{b}_o^s \otimes \mathbf{n}_o^s \tag{3}$$

where $\dot{\gamma}^s$ is the shear rate per slip system s, and $\mathbf{b}_o^s$, and $\mathbf{n}_o^s$ are the slip direction and slip plane normal, respectively, expressed in the total Lagrangian frame as indicated by the subscript 'o'. Given $\mathbf{F}^p$, $\mathbf{F}^*$ can be evaluated for Eq. (2).

The power-law relation is used for the shear rate as [72–76]

$$\dot{\gamma}^s = \dot{\gamma}_0^s \left(\frac{|\tau^s|}{\tau_c^s}\right)^{1/m} \mathrm{sign}(\tau^s) \tag{4}$$

where, τ^s is on the driving resolved shear stress ($\tau^s = \mathbf{T}^* : \mathbf{m}^s$ with $\mathbf{m}^s(\mathbf{x}) = 0.5(\mathbf{b}^s \otimes \mathbf{n}^s + \mathbf{n}^s \otimes \mathbf{b}^s)$) on the slip system s, τ_c^s is the critical resolved shear stress (CRSS) resistance to slip, $\dot{\gamma}_0^\alpha$ is a reference slip rate of 0.001 s^{-1}, and m is the strain rate sensitivity exponent of 0.05.

To capture texture evolution, the crystal lattice spin tensor, $\mathbf{W}^*$, is calculated using

$$\mathbf{W}^* = \mathbf{W}^{app} - \mathbf{W}^p,\ \mathbf{W}^p = \frac{1}{2}\left(\mathbf{L}^p - \mathbf{L}^{pT}\right) = \sum_s 0.5\dot{\gamma}^s\left(\mathbf{b}_o^s \otimes \mathbf{n}_o^s - \mathbf{n}_o^s \otimes \mathbf{b}_o^s\right) \tag{5}$$

where $\mathbf{W}^{app}$ is an imposed spin over the polycrystal driven by boundary conditions and $\mathbf{W}^p$ is the plastic spin due to shearing by crystallographic slip. The numerical implementation of the above theory within the weak form of the boundary value problem solved using the finite element method was presented in [70].

2.2. EVPFFT

In the small strain formulation of EVPFFT, the viscoplastic strain rate, $\dot{\boldsymbol{\varepsilon}}^p(\mathbf{x})$ is related to the Cauchy stress $\boldsymbol{\sigma}(\mathbf{x})$ at a material point $\mathbf{x}$ through a sum over slip systems [77,78]

$$\dot{\boldsymbol{\varepsilon}}^p(\mathbf{x}) = \sum_{s=1}^{N} \mathbf{m}^s(\mathbf{x})\dot{\gamma}^s(\mathbf{x}) = \dot{\gamma}_0 \sum_{s=1}^{N} \mathbf{m}^s(\mathbf{x})\left(\frac{|\mathbf{m}^s(\mathbf{x}) : \boldsymbol{\sigma}(\mathbf{x})|}{\tau_c^s(\mathbf{x})}\right)^n sgn(\mathbf{m}^s(\mathbf{x}) : \boldsymbol{\sigma}(\mathbf{x})), \tag{6}$$

where $\dot{\gamma}_0$ and $n = \frac{1}{m}$ are the same as in CPFE.

In EVPFFT, Hooke's law represents the elasto-plastic stress–strain constitutive relation:

$$\boldsymbol{\sigma}^{t+\Delta t}(\mathbf{x}) = \mathbf{C}(\mathbf{x}) : \boldsymbol{\varepsilon}^{e,t+\Delta t}(\mathbf{x}) = \mathbf{C}(\mathbf{x}) : (\boldsymbol{\varepsilon}^{t+\Delta t}(\mathbf{x}) - \boldsymbol{\varepsilon}^{p,t}(\mathbf{x}) - \dot{\boldsymbol{\varepsilon}}^{p,t+\Delta t}(\mathbf{x}, \boldsymbol{\sigma}^{t+\Delta t})\Delta t), \tag{7}$$

in which $\boldsymbol{\varepsilon}^e(\mathbf{x})$, $\boldsymbol{\varepsilon}^p(\mathbf{x})$, and $\boldsymbol{\varepsilon}(\mathbf{x})$ are the elastic, plastic, and total strain tensors, respectively. Using Eq. (7), the total strain is

$$\boldsymbol{\varepsilon}^{t+\Delta t}(\mathbf{x}) = \mathbf{C}^{-1}(\mathbf{x}) : \boldsymbol{\sigma}^{t+\Delta t}(\mathbf{x}) + \boldsymbol{\varepsilon}^{p,t}(\mathbf{x}) + \dot{\boldsymbol{\varepsilon}}^{p,t+\Delta t}(\mathbf{x}, \boldsymbol{\sigma}^{t+\Delta t})\Delta t. \tag{8}$$

In Green's approach, the elastic strain–stress constitutive relation is written as

$$\sigma_{ij}(\mathbf{x}) = \sigma_{ij}(\mathbf{x}) + C_{ijkl}^0 u_{k,l}(\mathbf{x}) - C_{ijkl}^0 u_{k,l}(\mathbf{x}), \tag{9}$$

where $u_{k,l}(\mathbf{x})$ is the displacement gradient tensor. Eq. (9) is

$$\sigma_{ij}(\mathbf{x}) = C_{ijkl}^0 u_{k,l}(\mathbf{x}) + \phi_{ij}(\mathbf{x}), \tag{10}$$

where the term $\phi_{ij}(\mathbf{x})$ is a polarization field as

$$\phi_{ij}(\mathbf{x}) = \sigma_{ij}(\mathbf{x}) - C_{ijkl}^0 u_{k,l}(\mathbf{x}). \tag{11}$$

Invoking the equilibrium,$\sigma_{ij,j}(\mathbf{x}) = 0$, Eq (10) yields the following governing equation

$$C_{ijkl}^0 u_{k,lj}(\mathbf{x}) + \phi_{ij,j}(\mathbf{x}) = 0. \tag{12}$$

Using Green's approach for Partial differential equation [79] by invoking Green's function $G_{km}(\mathbf{x})$ correlated with the displacement $u_k(\mathbf{x})$ we obtain

$$C_{ijkl}^0 G_{km,lj}(\mathbf{x} - \mathbf{x}') + \delta_{im}\delta(\mathbf{x} - \mathbf{x}') = 0. \tag{13}$$

After applying the convolution theorem [80] we get

$$\widetilde{u}_{k,l}(\mathbf{x}) = \int_{R^3} G_{ki,jl}(\mathbf{x} - \mathbf{x}')\phi_{ij}(\mathbf{x}')\, d\mathbf{x}'. \tag{14}$$

Solving Eq. (14) in the Fourier space and then obtaining an inverse transform to return into the real space, we obtain the strain as

$$\varepsilon_{ij}(\mathbf{x}) = E_{ij} + FT^{-1}\left(sym\left(\widehat{\Gamma}_{ijkl}^0(\mathbf{k})\right)\widehat{\phi}_{kl}(\mathbf{k})\right), \tag{15}$$

where "$\widehat{\ }$" and FT^{-1} symbols denote direct and inverse transforms, respectively. $\mathbf{k}$ enumerates the frequencies in the Fourier space. E_{ij} denotes the macro strain over the whole polycrystal by taking the average over a microstructural cell.

The fourth order tensor $\widehat{\Gamma}_{ijkl}^0(\mathbf{k})$ is

$$\widehat{\Gamma}_{ijkl}^0(\mathbf{k}) = -k_j k_l \widehat{G}_{ik}(\mathbf{k});\ \ \widehat{G}_{ik}(\mathbf{k}) = \left[C_{kjil}k_l k_j\right]^{-1}. \tag{16}$$

Numerical solution of Eq. (12) necessitates an iterative Newton Raphson procedure to obtain the stress and strain per voxel satisfying equilibrium and compatibility, as described in [12]. Texture evolution in EVPFFT is calculated the same way as in CPFE.

2.3. Hardening

The models summarized above incorporate the same hardening law for the evolution of slip resistance to facilitate fair comparisons [10]. The law is based on the evolution of statistically stored dislocations density governing the evolution of slip resistance, τ_c^s, per slip system belonging to $\{111\}\langle 110\rangle$ octahedral slip family. The τ_c^s is the sum of three contributions to the resistance [81–84]

$$\tau_c^s = \tau_0 + \tau_{for}^s + \tau_{sub} \tag{17}$$

where τ_0 is an initial friction stress assumed to embed the Peierls stress, barrier effect originating from grain size, and some initial dislocation density. The term does not evolve with plastic strain. The remaining two terms contribute to the evolution of slip resistance per slip system. The middle term is the forest, while the last term is the substructure/debris interaction stress. These two terms evolve with corresponding dislocation densities [85–88]

$$\tau_{for}^s = \chi b\mu\sqrt{\rho_{for}^s} \tag{18}$$

$$\tau_{sub} = 0.086\mu b\sqrt{\rho_{sub}}\log\left(\frac{1}{b\sqrt{\rho_{sub}}}\right) \tag{19}$$

where b is the Burgers vector (2.5563 × 10^{-10} m for Cu), μ is the shear modulus, and χ is an interaction factor for dislocations set to 0.9 [89]. The initial forest dislocation density is set to $\sum_s \rho_{0,for} = 10^{12}\,\mathrm{m}^{-2}$ resembling an annealed state of the material. ρ_{for}^s evolves using a balance between the rate of generation and the rate of dynamic recovery as [85,90–93]

$$\frac{\partial \rho_{for}^s}{\partial \gamma^s} = \frac{\partial \rho_{gen,for}^s}{\partial \gamma^s} - \frac{\partial \rho_{rem,for}^s}{\partial \gamma^s} = k_1\sqrt{\rho_{for}^s} - k_2(\dot{\varepsilon}, T)\rho_{for}^s,\ \Delta\rho_{for}^s = \frac{\partial \rho_{for}^s}{\partial \gamma^s}\Delta\gamma^s \tag{20}$$

where k_1 is a fitting coefficient for statistical trapping and k_2 is a rate-sensitive coefficient obtained using [94–97]

$$\frac{k_2}{k_1} = \frac{\chi b}{g}\left(1 - \frac{kT}{Db^3}\ln\left(\frac{\dot{\varepsilon}}{\dot{\varepsilon}_o}\right)\right) \tag{21}$$

In Eq. (12), k, $\dot{\varepsilon}_o$, g, and D are a constant of Boltzmann, a reference strain-rate set to $10^7\ s^{-1}$, an activation enthalpy as a fitting constant, and a drag stress as another fitting constant, respectively. The rate of debris dislocation density evolution follows

$$\Delta\rho_{sub} = qb\sqrt{\rho_{sub}}k_2\rho_{for}\sum_s|\Delta\gamma^s| \tag{22}$$

with q as a fitting constant determining a fraction of dislocations that lead to debris formation, while the rest is annihilated.

2.4. Calibration of the hardening law in CPFE and EVPFFT

The CPFE and EVPFFT models incorporating the same hardening law were calibrated to simulate the stress–strain response of polycrystalline copper. Consistent with the experiment, the calibration simulations were performed under a strain rate of 0.001 s^{-1} and at room temperature. Simple tension boundary conditions were imposed along a loading direction which is the rolling direction while enforcing zero stress along the two lateral directions over a rolling texture. The boundary conditions for CPFE were facilitated by running a one element simulation in Abaqus, while for EVPFFT a mixed Cauchy stress and strain rate boundary conditions were imposed over an appropriate microstructural cell.

The initial slip resistance, τ_0, trapping rate coefficient, k_1, activation barrier, g, drag stress, D, and rate coefficient q were fit to reproduce the stress–strain curve. First, τ_0 was fit to model yield stress. Next, k_1, was varied to model the initial hardening slope. Next, g and D were adjusted to match the hardening response. Finally, q was adjusted to capture the later stage of the hardening response. The hardening parameters are given in Table 1. Only one parameter was necessary to be different for EVPFFT from CPFE. Fig. 1 shows results of the calculations to reproduce the flow stress response of Cu. The models predict nearly identical stress–strain responses necessary for fair comparisons.

3. Microstructural cells and boundary conditions

Initial voxelated microstructural cells were generated in DREAM.3D according to the specifications in Table 2. Three resolutions of 67 grains were created to study heterogeneous deformation in ST, SS, and ST + SS. The middle resolution is shown in Fig. 2, as an example. The figure shows a selected grain completely embedded into the microstructure. The stair-stepped morphology decorating the grain is evident. The stair-stepped grain boundaries will be smoothed by meshing for CPFE. Mechanical fields would be influenced if such a hexahedral mesh with the stair-case grain boundaries is used as an input into a CPFE simulation. Unrealistic intense plasticity regions could arise as a result of stair-case morphologies as revealed in a study comparing stair-case versus smooth/flat grain boundaries [52]. Therefore smooth/flat grain boundary morphologies are highly recommended in CPFE simulations.

A numerical study using a CPFE model was performed in [52] to investigate the influence of the grain boundary morphology (stair-case versus smooth/flat) on the distribution of simulated mechanical fields. The study revealed that while the volume averaged responses showed no appreciable dependence on the grain boundary representation, the stair-case grain boundaries showed more extreme local plasticity values (i.e. heads and tails of the field distributions). Depending upon the level of the deformation compatibility between the grains neighboring each other, the simulation results showed that the grain boundary represented by the stair-case morphology can be sources and/or sinks for local extreme plasticity, compared to the grain boundary represented by the smooth (or flat) morphology. Increasing the mesh density can decrease the stair-case boundary effects and improve the discrepancy in local plasticity responses between the smooth and the stepped cases at the expanse of a prohibitive computational expense [51]. Nevertheless, the conformal discretization across interfaces eliminates such artificial stress localizations intrinsic to the non-conformal discretization. Therefore, interface conformal meshing is a way to go to eliminate artificial behavior owing to numerical discretization, which is especially important when attempting to model localized damage and failure.

Table 1
Model parameters fit to predict the curves in Fig. 1 using the CPFE and EVPFFT models.

	τ_0 [MPa]	D [MPa]	k_1 [m^{-1}]	g	q
EVPFFT	7	55	1.5x10^8	0.01	5
CPFE	7	87.5	1.5x10^8	0.01	5

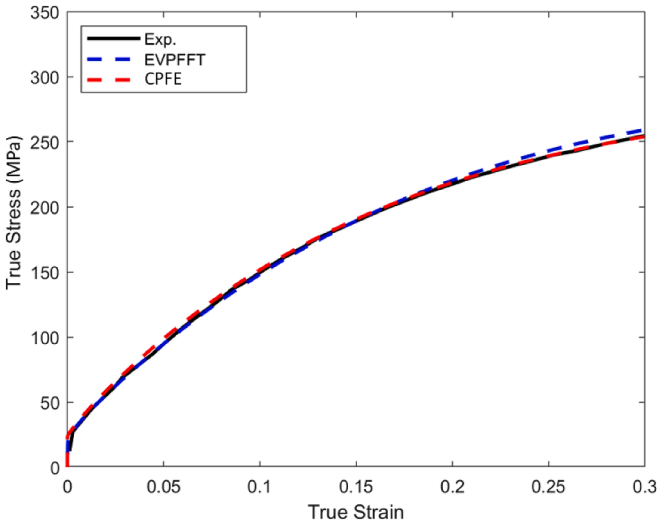

Fig. 1. Flow curves showing fits of the CPFE and EVPFFT calculated curves against the measured curve for polycrystalline Cu.

We relied on the Cubit/Sculpt meshing tool [59–61] to generate smooth and interface conformal hexahedral meshes of the polycrystalline structure from Fig. 2. The procedure began by forming grid nodes to approximate grain interfaces ensuring volume fractions of grains and then one or more hexahedra were inserted on both sides of the interfaces. To improve smoothness of the interfaces and the resulting quality of the hexahedra, one or multiple smoothing steps were then performed. The smoothing steps extend the time to generate hex mesh and make the procedure semi-automatic to obtain good mesh quality. A more detailed description of interface conformal meshing with hexahedral structural elements in Cubit/Sculpt can be found in [51,59].

Following our earlier work on mesh resolutions [63], two mesh densities, 'medium' and 'fine', were generated for the present work. The earlier work categorized meshes by an approximate number of IPs per mesh density (extra-coarse, coarse, medium, and fine). Six initial meshes per density were selected for the present numerical study of the following element types: 8-node linear brick (hex) (C3D8), 8-node linear brick with reduced integration (C3D8R), 20-node quadratic brick (C3D20), 20-node quadratic brick, which is hybrid with linear pressure (C3D20H), 20-node quadratic brick with reduced integration (C3D20R), and 20-node quadratic brick with reduced integration, which hybrid with linear pressure (C3D20RH).

The procedures described in [49] and later refined in [53] were followed to generate tetrahedral meshes. This procedure begins with triangular surface meshes of grains extracted as STL files from the hexahedral meshes. To this end, each rectangular element at grain boundaries was split over its diagonal to make the triangles. The STLs were then meshed in MSC Patran [98] with the internal element size

Table 2
Parameters of microstructural cells for the EVPFFT simulations.

	Number of grains	Number of voxels per cell	Average number of voxels per grain	Equivalent sphere diameter	Average aspect ratio of grains (a/b, a/c)	Voxel edge length	Cell dimensions
64^3	67	262,144	3,912	2.73	0.51	0.14	9x9x9
128^3	67	2,097,152	31,301	2.73	0.51	0.07	9x9x9
256^3	67	16,777,216	250,406	2.73	0.51	0.0351	9x9x9

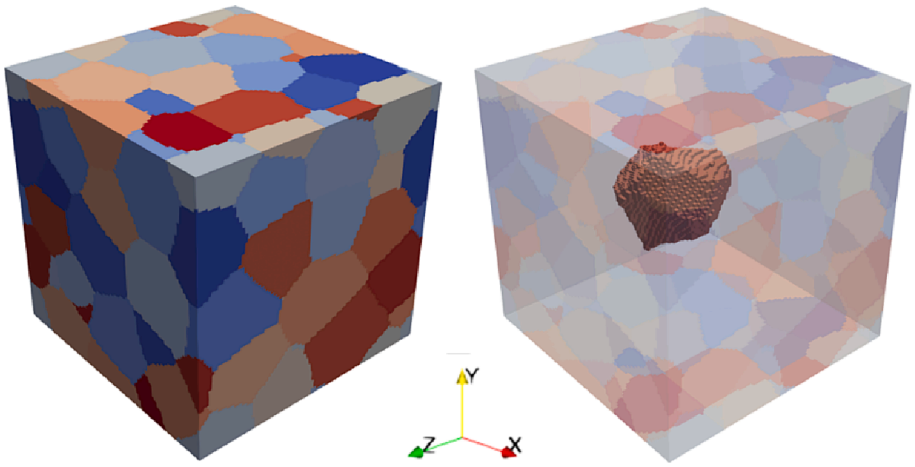

Fig. 2. A periodic polycrystalline microstructure consisting of 67 grains discretized into voxels. The image on the right shows the internal structure highlighting the selected central grain along with the stair-stepped morphology of the grain boundary voxels in the voxel-based microstructure. The edge length of the microstructural cell is taken as 9 (Table 2).

coarsening on. In contrast to hex mesh generation, the tet mesh generation is automatic and rapid. A total of three tetrahedral meshes per density were generated for the present numerical study of the following element types: 10-node quadratic tet (C3D10), 10-node quadratic tetrahedron, which is hybrid with linear pressure C3D10H, and 10-node modified tetrahedron with hourglass control, which is also hybrid with linear pressure (C3D10MH).

The meshes are shown in Fig. 3. Table 3 and Table 4 list characteristics of the meshes. Elements containing the same number of IPs are grouped together. The selected meshes of two resolutions and nine element types can facilitate a variety of comparisons in terms of accuracy of local and global mechanical fields during deformation, computational speed, and memory requirements as will be presented in subsequent sections of the paper. An RVE of a microstructure must have enough constituent grains to homogenize the variability of mechanical fields arising from local microstructural features. We point out that the 67 grains model used in the present work is not intended to be an RVE but a microstructural cell facilitating the numerical study. Pole figures depicting the distribution of crystal lattice orientations assigned to the model are shown in Fig. 4. There are 67 grains treated as separate element sets in the overall model. Each crystal orientation is randomly assigned to the sets.

Periodic boundary conditions were prescribed to all microstructural meshes, wherein the deformation of each pair of boundary faces (front/back, top/bottom, and left/right) is equal. Nodes belonging to each boundary face were made as a node-set to facilitate pairing between nodes on opposite faces. A node on the opposite face is found and tied to the first node on the given face and these are made as a node pair set. On top of the periodic boundary conditions, ST was prescribed as a combination of displacement in the positive Y direction and stress-free lateral surfaces. Likewise, on top of the periodic boundary conditions, SS boundary conditions were prescribed as displacement along the Y-direction on the positive Z face, while the negative Z face was constrained in the Y direction. The applied displacement in both ST and SS corresponded to the effective strain of 0.2 under a strain rate of 0.001 /s at room temperature. Finally, ST + SS boundary conditions were a combination of the ST boundary conditions to a strain of 0.1 and the SS boundary conditions from 0.1 to 0.2 strain.

Boundary conditions in EVPFFT are naturally periodic. Mixed Cauchy stress and velocity gradient boundary conditions are used to impose ST and SS identically as in CPFE. For example, ST boundary conditions were imposed with a velocity along a loading direction, while enforcing zero average stress along the two lateral directions over the microstructural cell.

4. Results

The CPFE model in the implicit finite element Abaqus Standard software was used to solve the boundary value problems of ST, SS, and ST + SS over the microstructural cell domains. A total of 54 (18 ST, 18 SS, and 18 ST + SS) simulations were performed and post-processed for this paper. Table 5 and Table 6 present the computational time needed to complete the jobs for the two mesh resolutions, respectively. The MPI parallel computing infrastructure of Abaqus was utilized, as indicated in the tables. Table 7 and Table 8 present the RAM memory needed to complete the jobs for the two resolutions, respectively. Memory usage is a function of the number of CPUs used in simulations. The CPFE model stores variables pertaining to the crystallography and the hardening law such as slip resistance and dislocation densities, in addition to the mechanical fields data. Evidently, the simulations were demanding in both RAM size requirement and computational time.

Given approximately the same number of IPs per mesh, the trends in computational time showed that C3D10 elements are the fastest of all element types explored in the work. C3D20R elements were found to also be very efficient and interestingly faster than C3D8 elements having the same number of IPs. Time requirements of C3D8R elements increased substantially relative to C3D8 elements given the overall number of IPs. The strain path change simulations took longer to complete than monotonic ST or SS simulations, especially for the quadratic hex elements. The quadratic hex elements were more memory

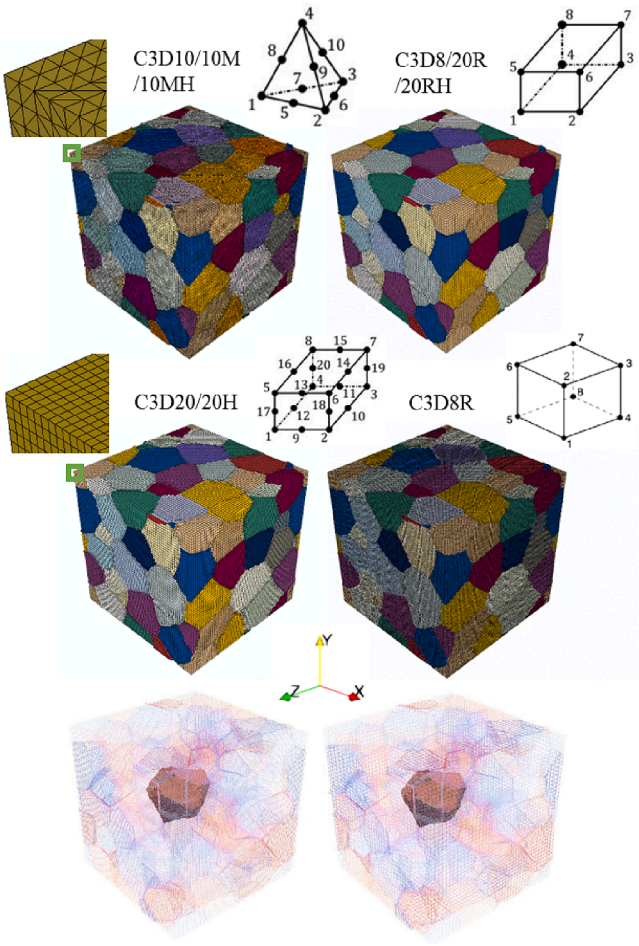

Fig. 3. (a) The same periodic polycrystalline microstructure as in Fig. 2 is discretized into different types of finite elements indicated in the figure. Grain boundaries in the FE models are conformal squares (hexahedral elements) and triangles (tetrahedral elements) representing grain boundary planes/curvatures shared between volume elements of neighboring grains. The images at bottom show the internal structure highlighting one central grain in tet (left) and brick (right) meshes. Quadratic tet (C3D10), linear brick (C3D8), and quadratic brick (C3D20) element schematics are shown. The edge length of the FE cubes is taken as 9.

Table 3
Characteristics of 'fine' meshes. The number of IPs for C3D8/20R/20RH elements is 8, for C3D10/10*H*/10MH elements is 4, for C3D20/20H elements is 27, and C3D8R elements is 1.

Element types	C3D8/20R/ 20RH	C3D10/ 10H/10MH	C3D20/ 20H	C3D8R
Number of elements per model	362,228	524,332	197,622	5,370,600
Average number of integration points per grain	43,248	31,304	79,650	80,158
Average number of elements per grain	5,406	7,826	2,950	80,158
Average element edge length	0.0126	0.0113	0.0158	0.0052
Degrees of freedom	1,133,379	2,786,493	5,035,791	12,673,439

demanding than linear hex elements. The hybrid element formulations took more time to complete the simulations. While the hybrid formulations required slightly more memory for every element type, the hourglass control hybrid tet elements, C3D10MH, appeared to be the most memory demanding, and much more than C3D10 and C3D10H

Table 4
Characteristics of 'medium' meshes. The number of IPs for C3D8/20R/20RH elements is 8, for C3D10/10*H*/10MH elements is 4, for C3D20/20H elements is 27, and C3D8R elements is 1.

Element types	C3D8/20R/ 20RH	C3D10/ 10H/10MH	C3D20/ 20H	C3D8R
Number of elements per model	331,908	156,526	87,962	2,196,565
Average number of integration points per grain	39,632	9,344	35,451	32,785
Average number of elements per grain	4,954	2,336	1,313	32,785
Average element edge length	0.0131	0.0169	0.0205	0.0075
Degrees of freedom	1,039,779	701,013	2,374,972	6,742,131

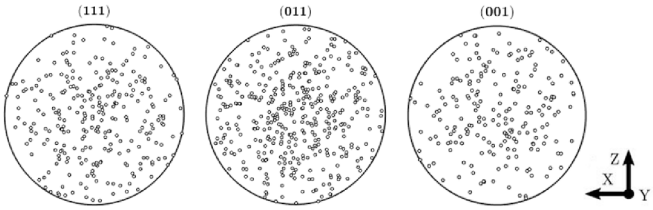

Fig. 4. Pole figures showing the distribution of 67 crystal orientations assigned to the models in Fig. 2 and 3.

elements. Like the time requirements, the memory requirements of C3D8R elements increased substantially relative to C3D8 elements given the overall number of IPs.

Figs. 5–7 show von-Mises stress, equivalent plastic strain, and pressure contours after ST, SS, and ST + SS to a macroscopic strain of 0.2. The fields vary owing to the different shape changes driven by the different boundary conditions. A view showing the fields at the surface and a section revealing the internal fields of the entire model as well as of the central grain are presented. The software ParaView was used for the visualization. To that end, Abaqus ODB files were converted into ParaView VTK files using the procedures described in [99].

Comparisons of the results with 'medium' and 'fine' resolutions revealed differences < 0.5 %. Given the independence on the level of discretization, only results of fine discretization are shown. Predicted strong/hot versus weak/cold spots in the microstructures of two resolutions were indistinguishable. Such predictions are not surprising based on our prior work in [63]. Also, the 'medium' grade meshes had element size like models used in several prior works in which mesh sensitivity studies were performed [49,100,101]. The 'fine' grade meshes were intended to further improve the accuracy of the simulations but evidently, the 'medium' grade meshes were already converged as the further refinement only slightly changed accuracy for < 0.5 %.

Evaluations of the fields as a function of element type showed that the fields predicted by C3D8 and C3D8R elements are not appreciably different. Softer fields and the smallest extent of the heterogeneities were predicted using the quadratic hex elements. The reduced integration hex elements, C3D20R and C3D20RH, slightly improved the sharpness of the fields relative to C3D20 and C3D20H elements. Quadratic tet elements predicted the fields like C3D8 elements. The sharpest predicted fields amongst the quadratic tet elements and nearly the same as those of C3D8 elements were those of C3D10MH elements. Quadratic hex elements predicted large range of values in pressure. Such large deviations are unrealistic and pose issues to the applicability of these elements in CPFE modeling of microstructures. Invoking the hybrid element formulation with constant pressure to possibly relax the issue did not help. The large range of values and underlying heterogeneity in the pressure fields relaxed with reduced integration. In summary, fields predicted by linear hex, quadratic hex with reduced

Table 5
Number of nodes x CPUs per node / total number of CPUs / total CPU time [h] / time per CPU [h] for the simulation cases using 'fine' meshes. One or multiple computer workstations of the type. Intel (R) - Xeon (R) - Gold 6130 CPU @ 2.10 GHz having 32 cores and 772 GB of RAM were used to perform the simulations.

Element types	C3D8	C3D20	C3D20R	C3D20RH	C3D20H	C3D10	C3D10H	C3D10MH	C3D8R
Tension	2x8/16/ 30.12/1.88	2x16/32/ 84.2/2.6	2x16/32/ 47.7/1.4	2x16/32/52.2/ 1.6	2x16/32/ 96.7/3.0	4x4/16/ 14.1/0.88	4x4/16/ 42.2/2.6	4x4/16/ 116.23/7.26	2x16/32/ 312.7/9.78
Shear	2x8/16/ 27.5/1.7	2x16/32/ 72.8/2.3	2x16/32/ 38.78/1.2	2x16/32/44.9/ 1.40	2x16/32/ 90.7/2.8	4x4/16/ 13.3/0.83	4x4/16/ 39.2/2.45	4x4/16/104.2/ 6.5	2x16/32/ 296.3/9.25
Tension + shear	2x8/16/ 30.4/1.90	2x16/32/ 113.9/3.6	2x16/32/ 94.53/2.95	2x16/32/ 116.2/3.6	2x16/32/ 132.2/4.1	4x4/16/ 20.0/1.25	4x4/16/ 47.3/2.95	4x4/16/122.2/ 7.63	2x16/32/ 339.2/10.6

Table 6
Number of nodes x CPUs per node / total number of CPUs / total CPU time [h] / time per CPU [h] for the simulation cases using 'medium' meshes. One or multiple computer workstations of the type. Intel (R) - Xeon (R) - Gold 6130 CPU @ 2.10 GHz having 32 cores and 772 GB of RAM were used to perform the simulations.

Element types	C3D8	C3D20	C3D20R	C3D20RH	C3D20H	C3D10	C3D10H	C3D10MH	C3D8R
Tension	2x8/16/ 22.7/1.41	2x16/32/ 48.9/1.5	2x16/32/28.8/ 0.9	2x16/32/33.9/ 1.06	2x16/32/ 62.3/1.9	4x4/16/ 16.23/1.0	4x4/16/23.2/ 1.45	4x4/16/96.73/ 6.04	2x16/32/ 221.5/6.92
Shear	2x8/16/ 22.4/1.4	2x16/32/ 40.1/1.25	2x16/32/ 27.23/0.85	2x16/32/33.4/ 1.04	2x16/32/ 53.3/1.6	4x4/16/9.78/ 0.611	4x4/16/19.2/ 1.2	4x4/16/90.08/ 5.63	2x16/32/ 219.5/6.85
Tension + shear	2x8/16/ 24.8/1.55	2x16/32/ 101.1/3.6	2x16/32/ 86.65/2.70	2x16/32/90.2/ 2.82	2x16/32/ 101.6/3.2	4x4/16/ 17.44/1.09	4x4/16/31.7/ 1.98	4x4/16/98.8/ 6.18	2x16/32/ 228.9/7.2

Table 7
Memory usage in GB per simulation case for 'fine' meshes.

Element types	C3D8	C3D20	C3D20R	C3D20RH	C3D20H	C3D10	C3D10H	C3D10MH	C3D8R
Tension	66.8	382.1	305.2	313.2	398.5	120.9	128.7	438.92	512.2
Shear	70.21	378.9	316.3	331.4	404.7	118.6	122.2	388.2	485.4
Tension + shear	77.32	380.6	313.2	328.9	401.2	118.6	122.4	492.2	509.9

Table 8
Memory usage in GB per simulation case for 'medium' meshes.

Element types	C3D8	C3D20	C3D20R	C3D20RH	C3D20H	C3D10	C3D10H	C3D10MH	C3D8R
Tension	57.4	303.8	281.6	292.5	311.4	28.22	30.6	352.7	438.3
Shear	57.43	288.8	281.6	298.8	326.8	36.32	38.4	376.7	412.9
Tension + shear	71.55	272	270.7	292	318.3	23.62	29.1	421.8	400.8

integration, and quadratic tetrahedral elements were similar with no issues arising in the pressure fields. Given that these observations are the same looking at ST, SS, or ST + SS, sensitivity on the boundary conditions was secondary.

Like CPFE in Abaqus, EVPFFT was also used to solve the same boundary value problems of ST, SS, and ST + SS over the microstructural cell domains. Table 9 shows the time involved in the simulations using three resolutions, while Table 10 shows the corresponding memory requirements. Given that the EVPFFT simulations were completed using a computing infrastructure involving GPUs, which is different from the infrastructure used for the CPFE simulations, the times are not compared. Such comparisons were performed in earlier works [67,102]. Fig. 8 shows the contours of von-Mises stress and equivalent plastic strain after ST, SS, and ST + SS. While there are some similarities in the fields predicted by CPFE and EVPFFT, there are also substantial differences at the strain of 0.2. Appendix A shows the comparisons at a strain of 0.02. The fields at 0.02 strain are much more similar meaning that the fields deviate with plastic strains. While the macroscopic behavior predicted by EVPFFT, through the stress–strain curves, is nearly insensitive to the degree by which interfaces between adjoining grains were numerically represented and resolved, differences in the local response evidently exist between voxelated versus conformal. Voxelated representation of the structures near interfaces yielded larger oscillations in the mechanical fields at grain boundaries. To relax these issues, methods of irregular discretization of microstructural domains are being developed for more accurate modeling using EVPFFT [103].

5. Discussion

Results of 54 large-scale CPFE simulations involving nine element types are used to discuss the effects of element type on accuracy and efficiency of the polycrystalline CPFE modeling. To the authors' knowledge, this is the first study comparing the solution accuracy and computational time as a function of element type in CPFE simulations of polycrystalline explicit grain structures. Insights from such a study are essential in predicting the evolutions of local fields during plastic deformation, especially for predicting phenomena such as void formations and propagation. The studies was challenging to perform as the simulations are not only computationally demanding but also require explicit meshing of grain structure using many elements of different types. In our work, the starting model was a voxel-based polycrystalline grain structure created synthetically in DREAM.3D. The voxel-based structure was then converted into the interface conformal hex and tet meshes relying on the software packages Cubit/Sculpt and Patran, respectively. Such interface conformal FE meshes are necessary for predicting localized behavior of polycrystals such as damage formation and failure. However, rapid generation of such 3D conformal meshes of polycrystalline microstructures is challenging, especially for hex elements because of the inherent difficulties in describing complex shapes with hex elements. To that end, the latest versions of Cubit/Sculpt are

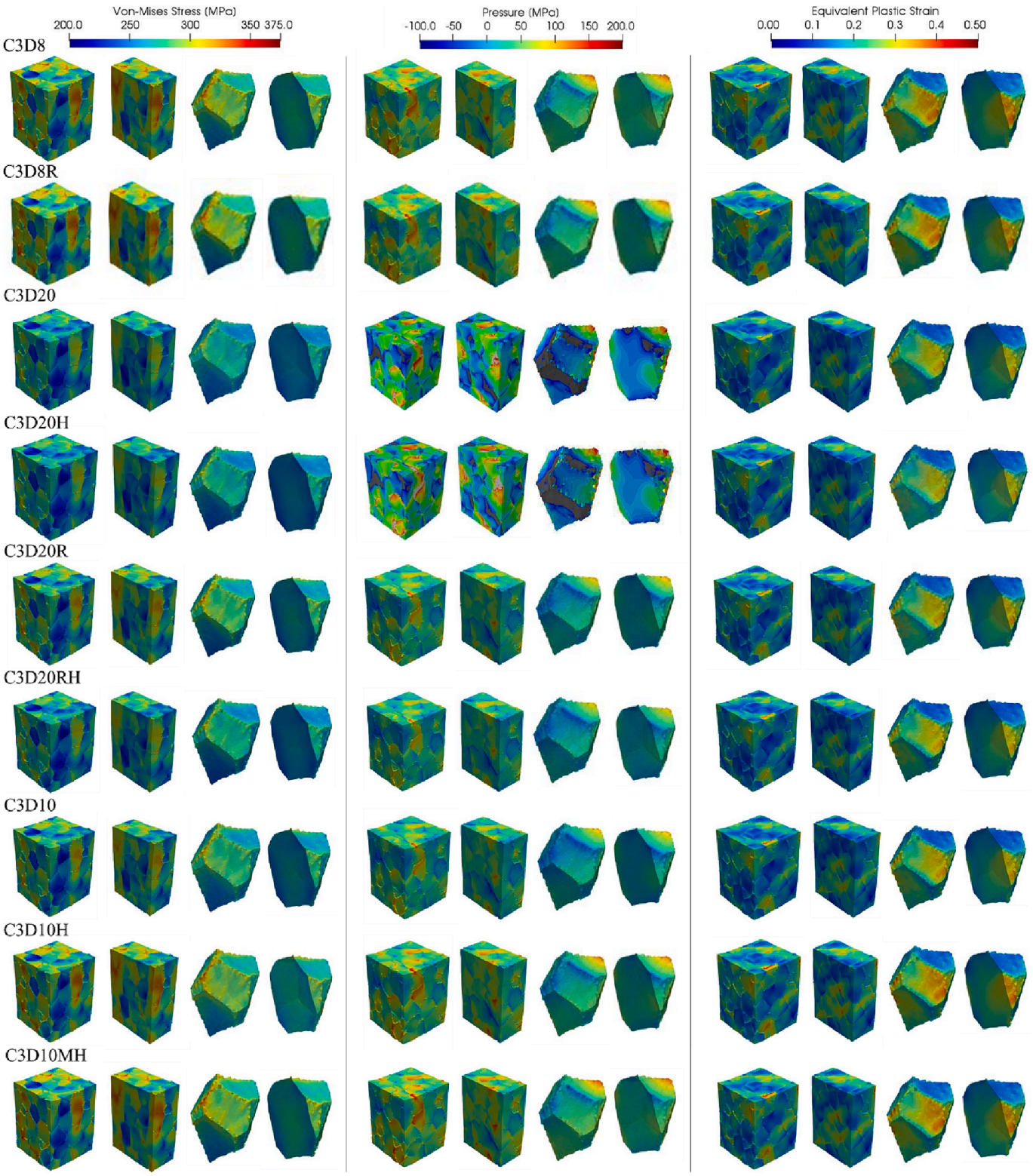

Fig. 5. Contours of von-Mises stress, pressure, and equivalent plastic strain after simple tension to an axial strain of 0.2 calculated using CPFE.

very advanced mesh generation tools. In contrast, tet elements are flexible for complex geometries.

Computing in parallel was utilized to run the jobs. The models with more elements required more time than smaller sized models, as expected. The computational time per CPU involved per simulation varied for every element type. The results showed that the time requirements varied for different boundary conditions per element type. In particular, the strain path change simulations took longer to complete for the quadratic hex elements than for other elements relative to tension and shear. The results further showed that C3D10 elements are the most efficient of all element types explored in the work. C3D20R elements were found to also be very efficient and interestingly faster than C3D8 elements. However, C3D20R elements were memory demanding. C3D8R elements increased both time and memory requirements

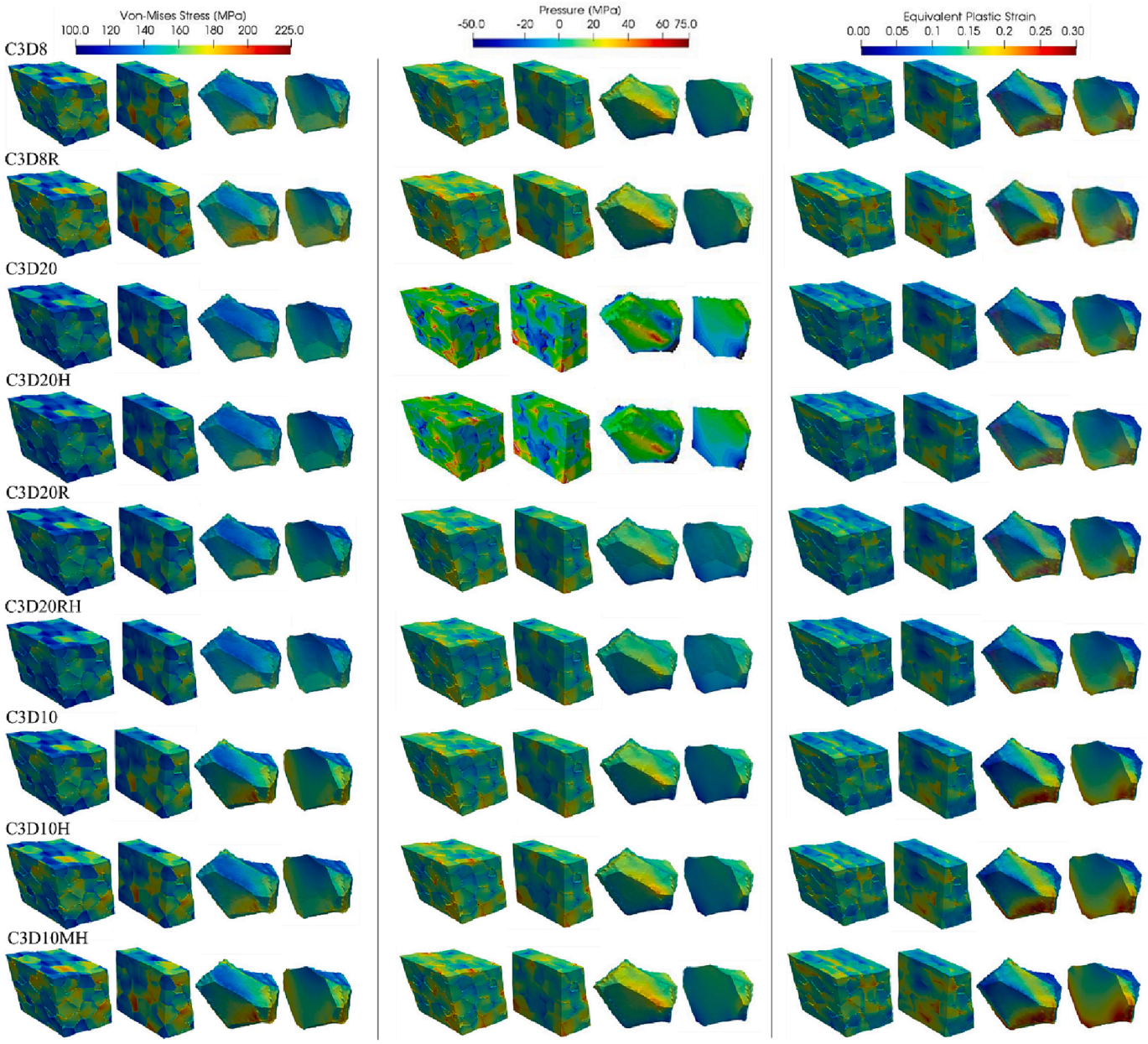

Fig. 6. Contours of von-Mises stress, pressure, and equivalent plastic strain after simple shear to a shear strain of 0.2 calculated using CPFE.

substantially relative to C3D8 elements. The hybrid element formulations required more time and memory to complete the simulations. In the hybrid formulation, the pressure stress is treated as an independent solution variable, coupled to the displacement solution through the constitutive theory. As a result, the hybrid formulation introduces more variables into the problem to alleviate the volumetric locking problem. The added variables make these elements more expensive. The hourglass control hybrid tet elements, C3D10MH, were the most time/memory demanding of all explored elements.

Simulation results in terms of predicted mechanical fields revealed strong functions of the element type. The fields predicted by C3D8 and C3D8R elements are about the same. In addition to being demanding as far as the computational time and memory, C3D8R elements are not recommended in some simulation cases due to their propensity to show the hourglass effect [104]. Hourglass effects can propagate easily through a mesh of first-order reduced integration elements, causing unreliable results. The effects are not a problem if multiple elements are used, e.g., at least four elements through the thickness in thin structures. Softer fields and the smallest extent of the heterogeneities were predicted using the quadratic hex elements. In general, the quadratic hex elements are not recommended for large distortions and plasticity [104]. According to the User Manual of Abaqus [104], the quadratic reduced-integration hex elements are more accurate than the corresponding fully-integrated elements. C3D20R and C3D20RH elements indeed improved the sharpness of the fields relative to C3D20 and C3D20H elements. While the fully integrated elements are not prone to exhibit the hourglass effect, the quadratic fully integrated hex elements are susceptible to volumetric locking, especially while modeling nearly or completely incompressible solids. C3D20 showed spurious pressure fields developed while enforcing the volume conservation. These elements are the most susceptible to lock with larger plastic strains. Invoking the hybrid element formulation with constant pressure, C3D20H did not fix the issue. However, the reduced-integration quadratic elements, C3D20R, successfully eliminated the issue. Although the reduced integration effectively eliminates volumetric locking in most problems with nearly incompressible material, hybrid

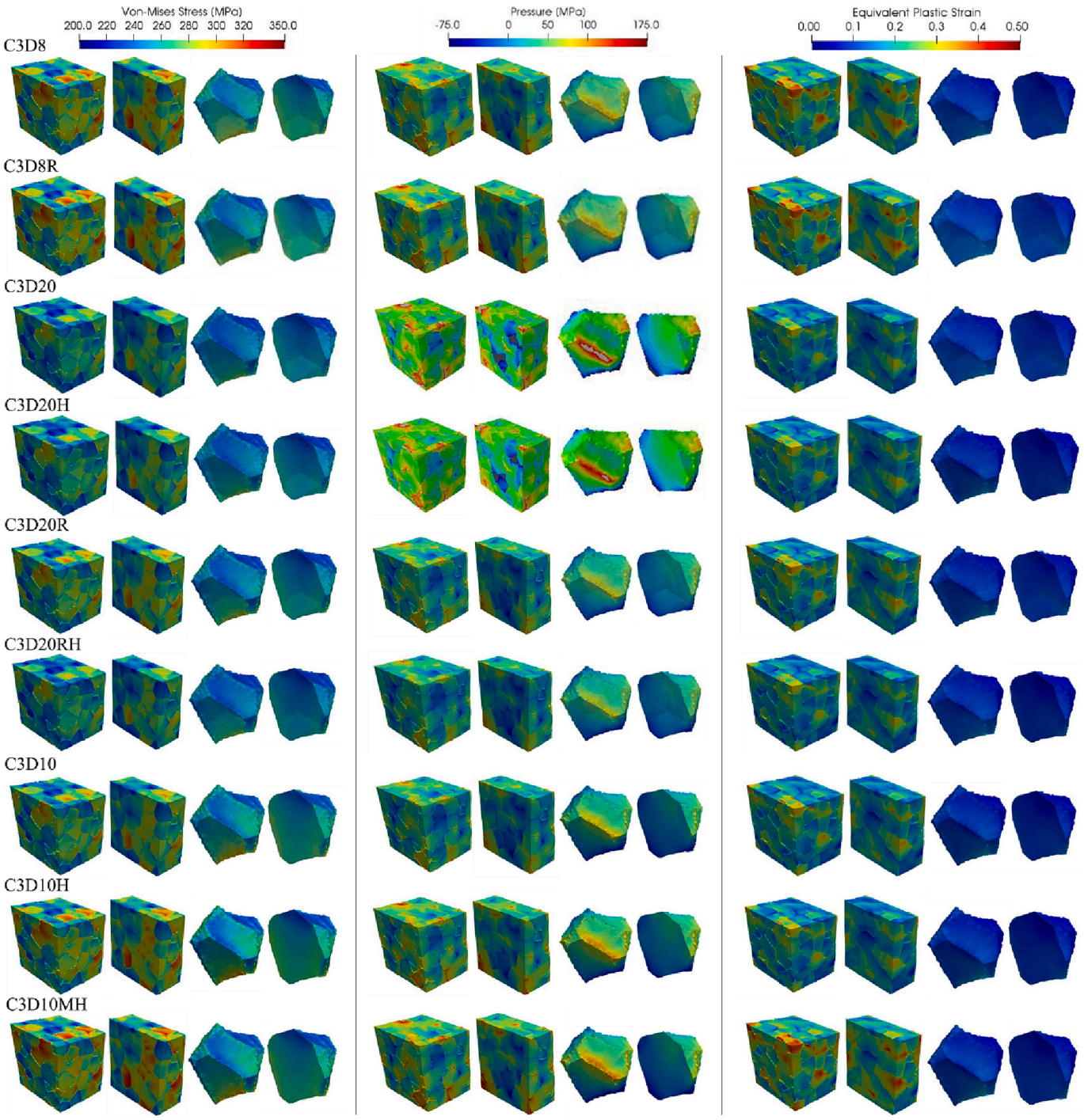

Fig. 7. Contours of von-Mises stress, pressure, and equivalent plastic strain after simple tension to an axial strain of 0.1 followed by simple shear to a shear strain of 0.1 calculated using CPFE.

Table 9
Number of nodes x GPUs per node / total time [h] / time per node [h] for the EVPFFT simulations. One or multiple computer workstations of the type. Intel (R) - Xeon (R) - Gold 6130 CPU @ 2.10 GHz having 32 cores and 772 GB of RAM were used to perform the simulations. The workstations incorporate an NVIDIA Tesla V100 GPU.

	Tension	Shear	Tension + shear
64^3	2x1/2.18/1.09	2x1/2.17/1.085	2x1/2.94/1.47
128^3	4x1/12.82/3.205	4x1/13.72/3.43	4x1/18.24/4.56
256^3	4x1/72.96/18.24	4x1/82.12/20.53	4x1/92.95/23.24

Table 10
Memory usage in GB per EVPFFT simulation case.

	Tension	Shear	Tension + shear
64^3	10.4	10.4	10.4
128^3	55.0	55.0	55.1
256^3	498.4	498.3	498.3

elements are recommended for meshes of reduced-integration elements that still show volumetric locking problems. Such problems can occur with elasto-plastic materials strained far into the plastic regimes. Nevertheless, the simulations run with C3D20RH in this work did not

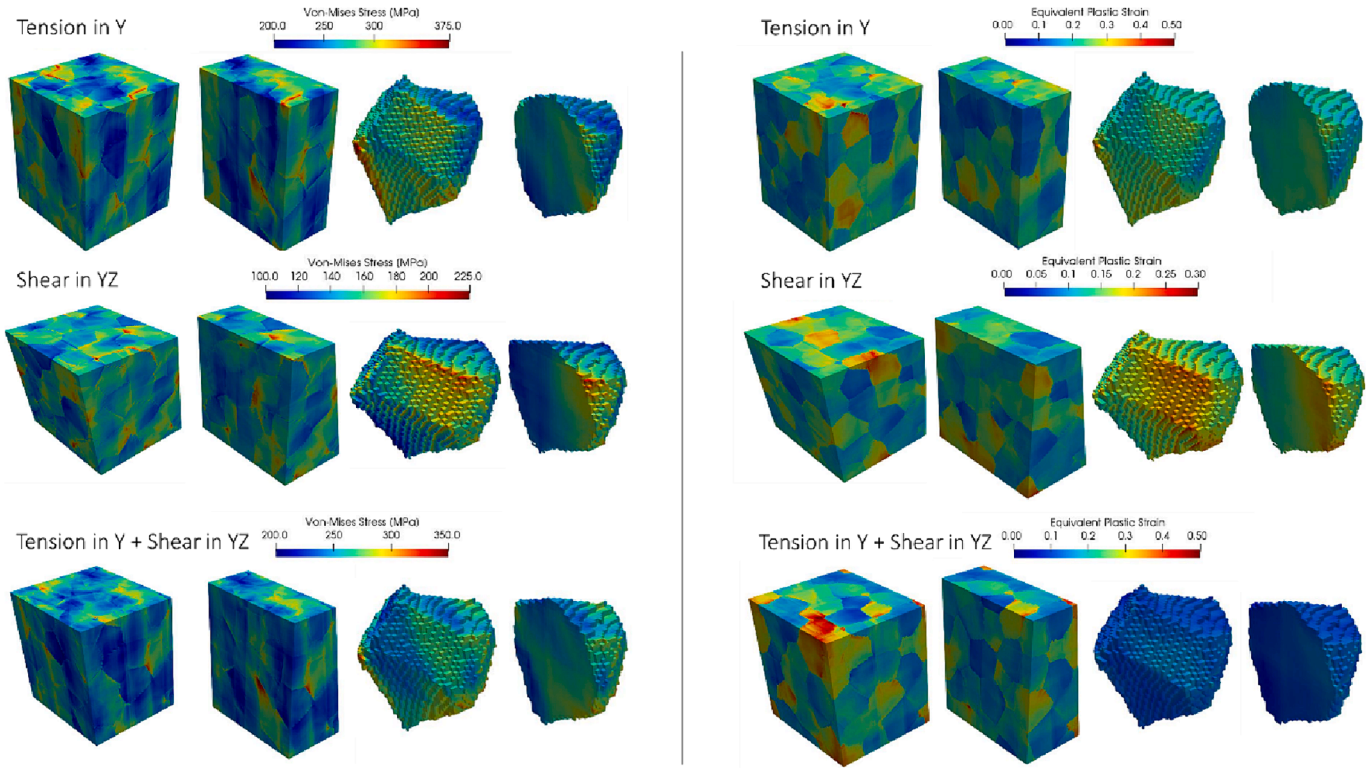

Fig. 8. Contours of von-Mises stress and equivalent plastic strain after simple tension to an axial strain of 0.2, simple shear to a shear strain of 0.2, and to an axial strain of 0.1 followed by simple shear of 0.1 calculated using EVPFFT.

show appreciable differences from those run with C3D20R, except for being a bit softer. Quadratic tet elements, C3D10, predicted the fields similar to C3D8 elements and also similar to C3D20R elements with no issues arising in the pressure fields. Our results suggest that these three element types are recommended for CPFE modeling of grain structures. Of the three, C3D10 elements are the most flexible to describe the shape of grains as the shapes are far from being rectangular for hex elements. Additionally, meshing with C3D10 elements is fully automatic.

To further confirm the qualitative observations described above, Fig. 9 compares the overall and local response in terms of major stress versus strain components from the nine CPFE and one EVPFFT simulations of ST and SS. Importantly, predictions of grain averaged stresses as shown in Fig. 9b can be validated using high energy synchrotron x-rays measurements. Such grain averaged quantities have been presented in [105]. The predicted variations imply that the hardening law parameters would vary depending on the selected element type for modeling. The figure confirms the qualitative observations that C3D8 elements produce the strongest response, right above the response produced by the C3D8R elements. The softest response is produced by C3D20 elements, while the reduced integration C3D20R elements slightly elevate the response. Quadratic tet elements produce the response in-between the stiff C3D8 and the compliant C3D20 elements. The response predicted by EVPFFT is the most similar to the response of C3D10 elements.

In closing, we attempt to quantify the difference in predicted fields using CPFE and EVPFFT. To this end, we calculate the stress deviations for CPFE and EVPFFT after simulating ST, SS, and ST + SS to a strain of 0.2. A vector of the normalized deviations for stress is evaluated using

$$\Delta\overline{\sigma}^k = \frac{\sqrt{(\boldsymbol{\sigma}^k - \overline{\boldsymbol{\sigma}}) : (\boldsymbol{\sigma}^k - \overline{\boldsymbol{\sigma}})}}{\sqrt{\frac{3}{2}\overline{\mathbf{s}} : \overline{\mathbf{s}}}} \text{ with } \overline{\mathbf{s}} = \overline{\boldsymbol{\sigma}} - \frac{tr(\overline{\boldsymbol{\sigma}})}{3}\mathbf{I} \tag{23}$$

where $\boldsymbol{\sigma}^k$ is stress at a voxel or an IP k, $\overline{\boldsymbol{\sigma}}$ is average stress over all voxels or IPs, and $\overline{\mathbf{s}}$ is the deviatoric stress. Histograms of von-Mises stress deviation are presented in Fig. 10. While averaged stresses are close, there are differences in local properties between CPFE and EVPFFT predictions. The intensity is slightly higher for CPFE, while the spread is slightly higher for EVPFFT. The origin of the differences is primarily in the formulations of the models. The EVPFFT model is formulated using small strains in an updated scheme, while CPFE is a finite strain total Lagrangian scheme model. The integral equations in finite elements are turned into the weak formulation, while the interactions in EVPFFT are handled by the Green's function. The evolution of voxels in EVPFFT is a uniform map during deformation, while finite elements change their shape in CPFE capturing nonlinearities. Likewise, the overall microstructural cell after deformation using EVPFFT preserves faces like individual voxels, while meshes result in irregular shapes. Grain boundaries are conformal in CPFE, while stair-stepped in EVPFFT.

6. Conclusions

Large-scale CPFE simulations were performed to evaluate the suitability of nine element types for the modeling of explicit grain structures. A voxel-based polycrystalline grain structure was generated in DREAM.3D and converted to interface conformal hexahedral elements using Cubit/Sculpt and interface conformal tetrahedral elements using Patran of two resolutions. Simple tension, simple shear, and a strain path change deformation involving simple tension and simple shear conditions were simulated using nine element types. The same simulations were performed using EVPFFT to facilitate comparisons. Post-processing of the simulation results allowed us to draw the following conclusions:

- The quadratic tet elements offer the best compromise between accuracy, efficiency, memory requirements, and flexibility to describe complex geometries for CPFE simulation of explicit microstructures. Moreover, these elements are suitable for rapid and automatic mesh generation algorithms. Amongst the explored elements, these elements predict the overall response the most similar to EVPFFT. The

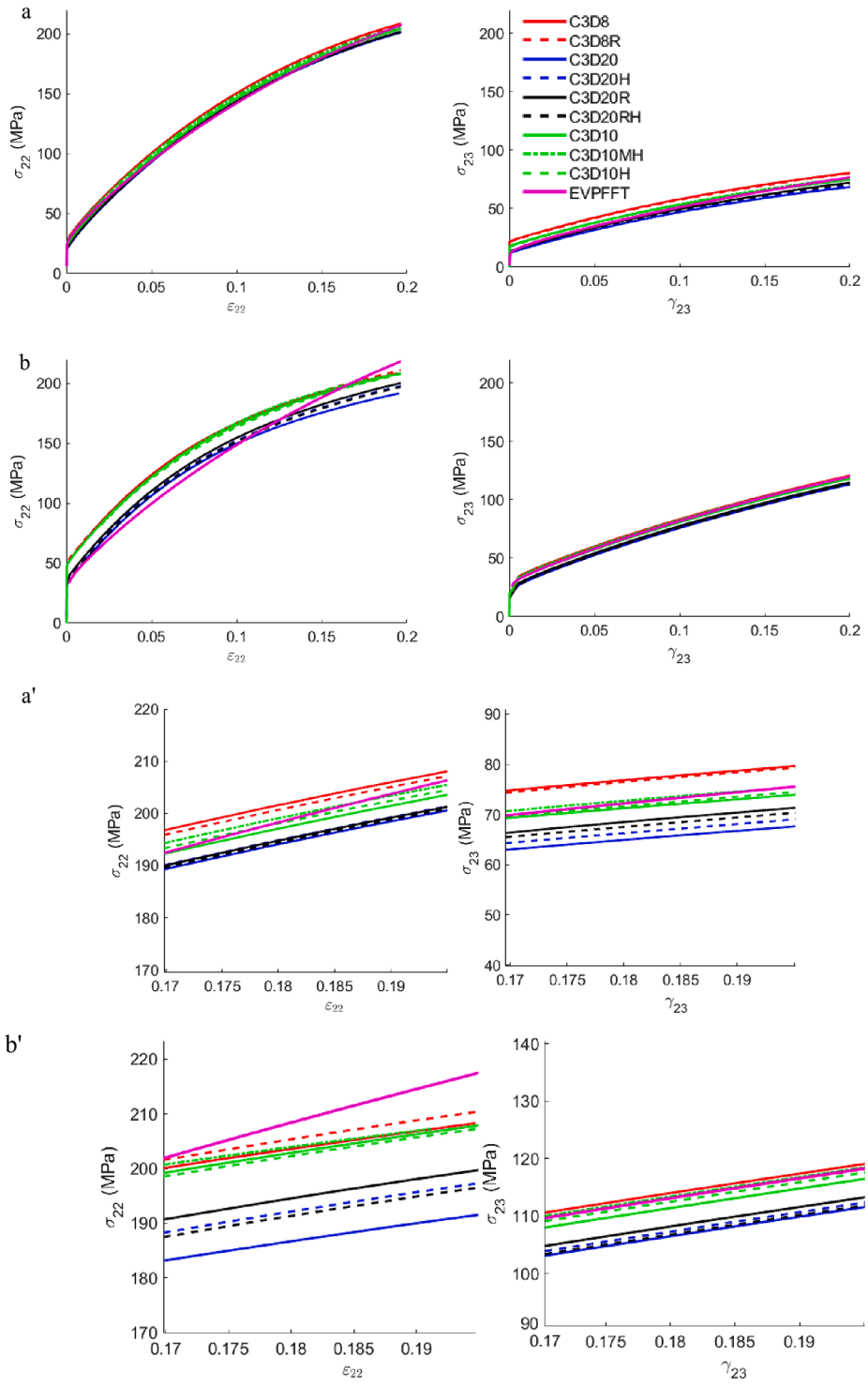

Fig. 9. (a) Overall and (b) central grain stress - strain response for simple tension (left) and simple shear (right). (a') and (b') are zoom in inserts at the ends of deformation.

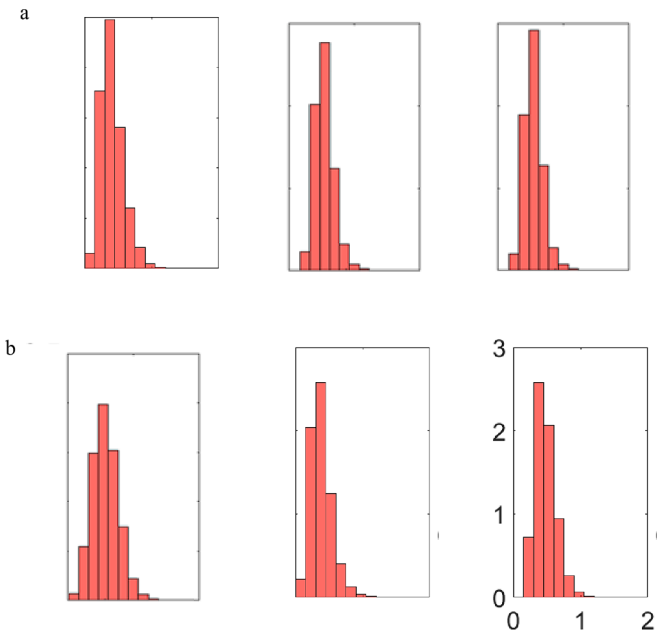

Fig. 10. Histograms of von-Mises stress deviation after simple tension to an axial strain of 0.2 (left), simple shear to a shear strain of 0.2 (middle), and simple tension to an axial strain of 0.1 followed by simple shear to a shear strain of 0.1 (right) predicted using (a) CPFE (C3D10) and (b) EVPFFT.

response is in between the stiff linear hex and compliant quadratic hex elements.

- Linear hex elements and quadratic hex elements with reduced integration are recommended for modeling nearly incompressible solids. While linear hex elements are an acceptable choice for CPFE modeling of explicit microstructures owing to their accuracy, efficiency, and memory requirements, the quadratic hex elements with reduced integration arise as the second choice for CPFE simulations owing to their accuracy and computational efficiency but require more memory. Although recommended for high mesh distortions in bulk metal forming, the linear hex elements with reduced integration increase both time and memory requirements substantially relative to the fully integrated linear hex elements for a given number of IPs.
- The quadratic hex elements are not suitable for large plastic deformation of complex grain structures due to their propensity to volumetric locking. While the hybrid formulation elements with constant pressure could not relax the issue, the quadratic hex elements with reduced integration fix the issue of volumetric locking. The hourglass control elements substantially increase the computational time and memory requirements.
- Different element types predict not only the local response to vary but also the overall response to vary. The predicted variation in the overall response implies that the hardening law parameters would also vary depending on the selected element type requiring calibration for every element type selected for modeling. While EVPFFT predicts the overall response similar to CPFE, especially to the quadratic tet elements, the predicted local fields deviate from those predicted by CPFE for all element types. The deviations increase with plastic strain.

It is anticipated that these conclusions provide useful guidance for CPFE modeling of explicit grain structures. As a specific crystal plasticity model formulation has minor effects on a selected element type, the guidance above should be applicable to any crystal plasticity model. Numerical analyses into the effects of element type on the localized phenomena at grain boundaries, other defects, and crack tips like in [106] will be studied in future works after advancing our models into strain gradient-based formulations considering geometrically necessary dislocations. Conducting such study would be essential since the strain gradient plasticity formulations exhibit strong sensitivity to both element type and mesh size as nonphysical values of geometrically necessary dislocation densities can lead to severe errors of local field quantities [107,108]. Mapping of not only mechanical fields but also microstructural evolution characteristics and underlying statistical analyses like in [109] will be pursued.

CRediT authorship contribution statement

Jacob Weiss: Formal analysis, Investigation, Validation, Visualization, Methodology. **Marko Knezevic:** Conceptualization, Funding acquisition, Project administration, Resources, Supervision, Writing – original draft, Writing – review & editing.

Declaration of competing interest

The authors declare that they have no known competing financial interests or personal relationships that could have appeared to influence the work reported in this paper.

Data availability

Data will be made available on request.

Acknowledgements

This work is based on a project no. CMMI-2118557 sponsored by the U.S. National Science Foundation. The authors acknowledge Elise Baribault-Lee for performing the EVPFFT simulations.

Appendix A

This appendix presents comparisons of the mechanical fields predicted by CPFE and EVPFFT at a strain of 0.02 (Fig. A1).

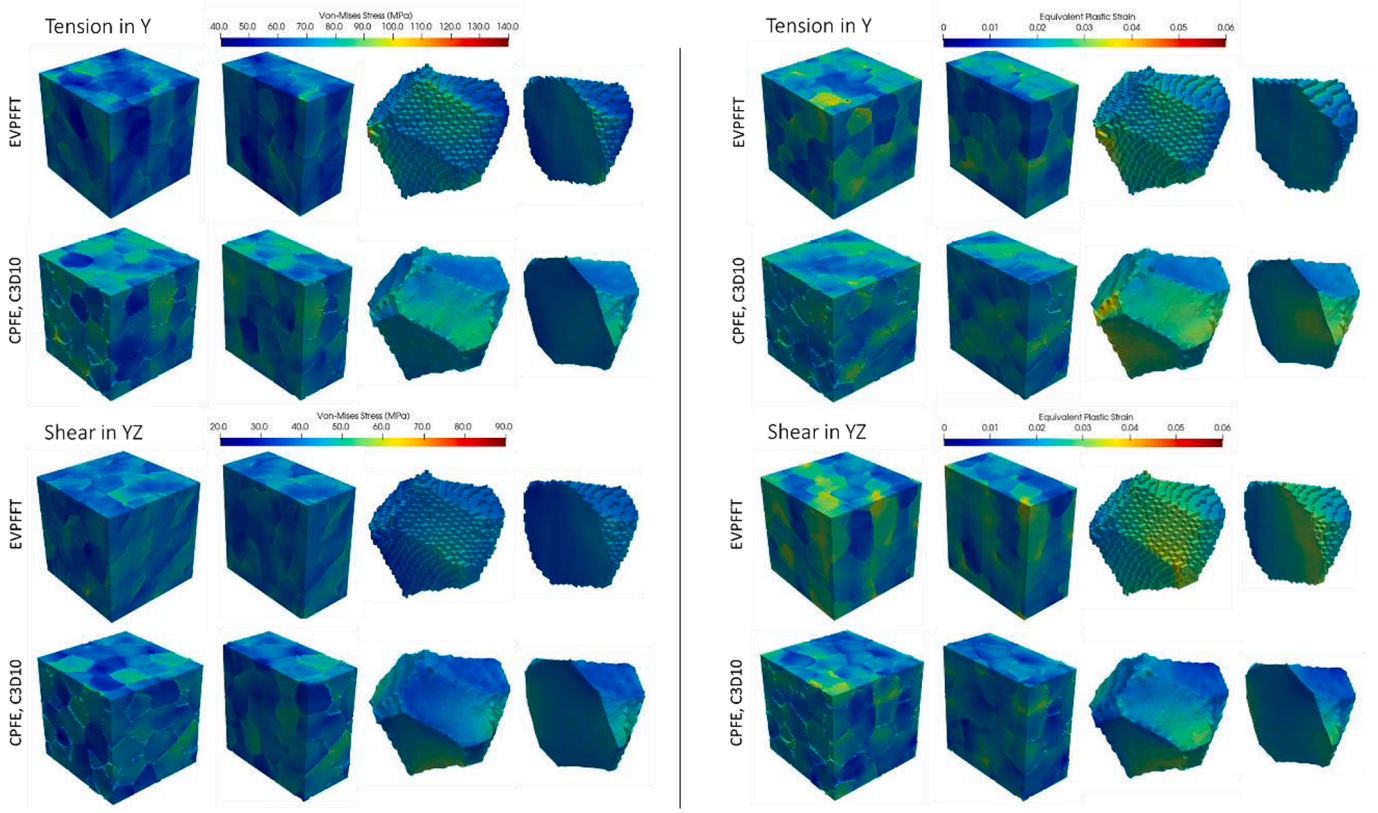

Fig. A1. Contours of von-Mises stress and equivalent plastic strain after simple tension to an axial strain of 0.02 and simple shear to a shear strain of 0.02 calculated using CPFE and EVPFFT.

References

[1] A. Eghtesad, M. Zecevic, R.A. Lebensohn, R.J. McCabe, M. Knezevic, Spectral database constitutive representation within a spectral micromechanical solver for computationally efficient polycrystal plasticity modelling, Comput. Mech. 61 (2018) 89–104.

[2] K.-J. Bathe, Finite element procedures, Englewood cliffs, Prentice Hall, N.J., 1996.

[3] M. Zecevic, M. Knezevic, A new visco-plastic self-consistent formulation implicit in dislocation-based hardening within implicit finite elements: application to high strain rate and impact deformation of tantalum, Computer Methods in Applied Mechanics and Engineering 341 (2018) 888–916.

[4] M. Zecevic, I.J. Beyerlein, M. Knezevic, Coupling elasto-plastic self-consistent crystal plasticity and implicit finite elements: applications to compression, cyclic tension-compression, and bending to large strains, Int. J. Plast. 93 (2017) 187–211.

[5] M. Zecevic, R.J. McCabe, M. Knezevic, A new implementation of the spectral crystal plasticity framework in implicit finite elements, Mechanics of Materials 84 (2015) 114–126.

[6] M. Zecevic, R.J. McCabe, M. Knezevic, Spectral database solutions to elasto-viscoplasticity within finite elements: application to a cobalt-based FCC superalloy, Int. J. Plast. 70 (2015) 151–165.

[7] D. Peirce, R.J. Asaro, A. Needleman, An analysis of nonuniform and localized deformation in ductile single crystals, Acta Metall. 30 (1982) 1087–1119.

[8] T.J. Barrett, M. Knezevic, Deep drawing simulations using the finite element method embedding a multi-level crystal plasticity constitutive law: Experimental verification and sensitivity analysis, Computer Methods in Applied Mechanics and Engineering 354 (2019) 245–270.

[9] R.A. Lebensohn, N-site modeling of a 3D viscoplastic polycrystal using fast fourier transform, Acta. Mater. 49 (2001) 2723–2737.

[10] M. Jahedi, M. Ardeljan, I.J. Beyerlein, M.H. Paydar, M. Knezevic, Enhancement of orientation gradients during simple shear deformation by application of simple compression, J. Appl. Phys. 117 (2015) 214309.

[11] H. Lim, J.D. Carroll, C.C. Battaile, T.E. Buchheit, B.L. Boyce, C.R. Weinberger, Grain-scale experimental validation of crystal plasticity finite element simulations of tantalum oligocrystals, Int. J. Plast. 60 (2014) 1–18.

[12] R.A. Lebensohn, A.K. Kanjarla, P. Eisenlohr, An elasto-viscoplastic formulation based on fast fourier transforms for the prediction of micromechanical fields in polycrystalline materials, Int. J. Plast. 32–33 (2012) 59–69.

[13] A. Eghtesad, T.J. Barrett, K. Germaschewski, R.A. Lebensohn, R.J. McCabe, M. Knezevic, OpenMP and MPI implementations of an elasto-viscoplastic fast fourier transform-based micromechanical solver for fast crystal plasticity modeling, Advances in Engineering Software 126 (2018) 46–60.

[14] A. Eghtesad, K. Germaschewski, M. Knezevic, Coupling of a multi-GPU accelerated elasto-visco-plastic fast fourier transform constitutive model with the implicit finite element method, Comput. Mater. Sci. 208 (2022) 111348.

[15] A. Eghtesad, K. Germaschewski, R.A. Lebensohn, M. Knezevic, A multi-GPU implementation of a full-field crystal plasticity solver for efficient modeling of high-resolution microstructures, Computer Physics Communications 254 (2020) 107231.

[16] A. Eghtesad, M. Knezevic, Modeling cyclic plasticity of additively manufactured alloy Mar-M-509 using a high-performance spectral-based micromechanical model, Applications in Engineering Science 7 (2021) 100065.

[17] A. Eghtesad, M. Knezevic, A full-field crystal plasticity model including the effects of precipitates: application to monotonic, load reversal, and low-cycle fatigue behavior of inconel 718, Mater. Sci. Eng. A 803 (2021) 140478.

[18] O. Diard, S. Leclercq, G. Rousselier, G. Cailletaud, Distribution of normal stress at grain boundaries in multicrystals: application to an intergranular damage modeling, Comput. Mater. Sci. 25 (2002) 73–84.

[19] Z. Zhao, M. Ramesh, D. Raabe, A.M. Cuitiño, R. Radovitzky, Investigation of three-dimensional aspects of grain-scale plastic surface deformation of an aluminum oligocrystal, Int. J. Plast. 24 (2008) 2278–2297.

[20] S.R. Kalidindi, A. Bhattacharya, R. Doherty, Detailed Analysis of Plastic Deformation in Columnar Polycrystalline Aluminum Using Orientation Image Mapping and Crystal Plasticity Models, Proceedings of the Royal Society of London: Mathematical, Physical and Engineering Sciences., 460 (2004) 1935 - 1956.

[21] H. Lim, J.D. Carroll, C.C. Battaile, B.L. Boyce, C.R. Weinberger, Quantitative comparison between experimental measurements and CP-FEM predictions of plastic deformation in a tantalum oligocrystal, International Journal of Mechanical Sciences 92 (2015) 98–108.

[22] M.A. Groeber, M.A. Jackson, Dream., 3D: a digital representation environment for the analysis of microstructure in 3D, integrating materials and Manufacturing, Innovation 3 (2014) 5.

[23] M. De Berg, M. Van Kreveld, M. Overmars, O.C. Schwarzkopf, Computational geometry, Springer, 2000.

[24] M. Shenoy, Y. Tjiptowidjojo, D. McDowell, Microstructure-sensitive modeling of polycrystalline IN 100, Int. J. Plast. 24 (2008) 1694–1730.

[25] O. Diard, S. Leclercq, G. Rousselier, G. Cailletaud, Evaluation of finite element based analysis of 3D multicrystalline aggregates plasticity: application to crystal plasticity model identification and the study of stress and strain fields near grain boundaries, Int. J. Plast. 21 (2005) 691–722.

[26] P. Zhang, M. Karimpour, D. Balint, J. Lin, Three-dimensional virtual grain structure generation with grain size control, Mechanics of Materials 55 (2012) 89–101.
[27] B. Boots, The arrangement of cells in “random” networks, Metallography 15 (1982) 53–62.
[28] D. Aboav, The arrangement of grains in a polycrystal, Metallography 3 (1970) 383–390.
[29] A. Rollett, D. Raabe, A hybrid model for mesoscopic simulation of recrystallization, Comput. Mater. Sci. 21 (2001) 69–78.
[30] A.D. Rollett, Overview of modeling and simulation of recrystallization, Prog. Mater. Sci. 42 (1997) 79–99.
[31] L.-Q. Chen, Phase-field models for microstructure evolution, Annual Review of Materials Research 32 (2002) 113–140.
[32] D. Raabe, Introduction of a scalable three-dimensional cellular automaton with a probabilistic switching rule for the discrete mesoscale simulation of recrystallization phenomena, Philosophical Magazine A 79 (1999) 2339–2358.
[33] V. Marx, F.R. Reher, G. Gottstein, Simulation of primary recrystallization using a modified three-dimensional cellular automaton, Acta. Mater. 47 (1999) 1219–1230.
[34] N. Zaafarani, D. Raabe, R. Singh, F. Roters, S. Zaefferer, Three-dimensional investigation of the texture and microstructure below a nanoindent in a cu single crystal using 3D EBSD and crystal plasticity finite element simulations, Acta. Mater. 54 (2006) 1863–1876.
[35] M. Calcagnotto, D. Ponge, E. Demir, D. Raabe, Orientation gradients and geometrically necessary dislocations in ultrafine grained dual-phase steels studied by 2D and 3D EBSD, Mater. Sci. Eng. A 527 (2010) 2738–2746.
[36] A. Khorashadizadeh, D. Raabe, S. Zaefferer, G. Rohrer, A. Rollett, M. Winning, Five-Parameter grain Boundary analysis by 3D EBSD of an ultra fine grained CuZr alloy processed by Equal Channel Angular pressing, Advanced Engineering Materials 13 (2011) 237–244.
[37] S. Zaefferer, S. Wright, D. Raabe, Three-dimensional orientation microscopy in a focused ion beam–scanning electron microscope: a new dimension of microstructure characterization, Metall. Mater. Trans. A 39 (2008) 374–389.
[38] S. Yi, I. Schestakow, S. Zaefferer, Twinning-related microstructural evolution during hot rolling and subsequent annealing of pure magnesium, Mater. Sci. Eng. A 516 (2009) 58–64.
[39] M.D. Uchic, M.A. Groeber, D.M. Dimiduk, J.P. Simmons, 3D microstructural characterization of nickel superalloys via serial-sectioning using a dual beam FIB-SEM, Scr. Mater. 55 (2006) 23–28.
[40] J.E. Spowart, H.E. Mullens, B.T. Puchala, Collecting and analyzing microstructures in three dimensions: a fully automated approach, JOM 55 (2003) 35–37.
[41] J.E. Spowart, Automated serial sectioning for 3-D analysis of microstructures, Scr. Mater. 55 (2006) 5–10.
[42] S.F. Li, J. Lind, C.M. Hefferan, R. Pokharel, U. Lienert, A.D. Rollett, R.M. Suter, Three-dimensional plastic response in polycrystalline copper via near-field high-energy X-ray diffraction microscopy, Journal of Applied Crystallography 45 (2012) 1098–1108.
[43] J. Lind, S.F. Li, R. Pokharel, U. Lienert, A.D. Rollett, R.M. Suter, Tensile twin nucleation events coupled to neighboring slip observed in three dimensions, Acta. Mater. 76 (2014) 213–220.
[44] C.A. Stein, A. Cerrone, T. Ozturk, S. Lee, P. Kenesei, H. Tucker, R. Pokharel, J. Lind, C. Hefferan, R.M. Suter, A.R. Ingraffea, A.D. Rollett, Fatigue crack initiation, slip localization and twin boundaries in a nickel-based superalloy, Current Opinion in Solid State and Materials Science 18 (2014) 244–252.
[45] W. Ludwig, S. Schmidt, E.M. Lauridsen, H.F. Poulsen, X-ray diffraction contrast tomography: a novel technique for three-dimensional grain mapping of polycrystals. I. Direct beam case, Journal of Applied Crystallography 41 (2008) 302–309.
[46] G. Johnson, A. King, M.G. Honnicke, J. Marrow, W. Ludwig, X-ray diffraction contrast tomography: a novel technique for three-dimensional grain mapping of polycrystals. II. the combined case, Journal of Applied Crystallography 41 (2008) 310–318.
[47] N.C. Ferreri, Z. Feng, D.J. Savage, D.W. Brown, B. Clausen, T.A. Sisneros, M. Knezevic, In-situ high-energy X-ray diffraction and crystal plasticity modeling to predict the evolution of texture, twinning, lattice strains and strength during loading and reloading of beryllium, Int. J. Plast. 150 (2022) 103217.
[48] T.J. Barrett, R.J. McCabe, D.W. Brown, B. Clausen, S.C. Vogel, M. Knezevic, Predicting deformation behavior of α-uranium during tension, compression, load reversal, rolling, and sheet forming using elasto-plastic, multi-level crystal plasticity coupled with finite elements, J. Mech. Phys. Solids 138 (2020) 103924.
[49] M. Knezevic, B. Drach, M. Ardeljan, I.J. Beyerlein, Three dimensional predictions of grain scale plasticity and grain boundaries using crystal plasticity finite element models, Computer Methods in Applied Mechanics and Engineering 277 (2014) 239–259.
[50] S.M. Qidwai, D.M. Turner, S.R. Niezgoda, A.C. Lewis, A.B. Geltmacher, D. J. Rowenhorst, S.R. Kalidindi, Estimating the response of polycrystalline materials using sets of weighted statistical volume elements, Acta. Mater. 60 (2012) 5284–5299.
[51] H. Lim, F. Abdeljawad, S.J. Owen, B.W. Hanks, J.W. Foulk, C.C. Battaile, Incorporating physically-based microstructures in materials modeling: bridging phase field and crystal plasticity frameworks, Modelling and Simulation in Materials Science and Engineering 24 (2016) 045016.
[52] Y.S. Choi, M.A. Groeber, T.J. Turner, D.M. Dimiduk, C. Woodward, M.D. Uchic, T. A. Parthasarathy, A crystal-plasticity FEM study on effects of simplified grain representation and mesh types on mesoscopic plasticity heterogeneities, Mater. Sci. Eng. A 553 (2012) 37–44.
[53] T.J. Barrett, D.J. Savage, M. Ardeljan, M. Knezevic, An automated procedure for geometry creation and finite element mesh generation: application to explicit grain structure models and machining distortion, Comput. Mater. Sci. 141 (2018) 269–281.
[54] S. Wang, W. Zhuang, J. Cao, J. Lin, An investigation of springback scatter in forming ultra-thin metal-sheet channel parts using crystal plasticity FE analysis, The International Journal of Advanced Manufacturing Technology 47 (2010) 845–852.
[55] W. Zhuang, S. Wang, J. Cao, J. Lin, C. Hartl, Modelling of localised thinning features in the hydroforming of micro-tubes using the crystal-plasticity FE method, The International Journal of Advanced Manufacturing Technology 47 (2010) 859–865.
[56] M. Ardeljan, M. Knezevic, T. Nizolek, I.J. Beyerlein, N.A. Mara, T.M. Pollock, A study of microstructure-driven strain localizations in two-phase polycrystalline HCP/BCC composites using a multi-scale model, Int. J. Plast. 74 (2015) 35–57.
[57] M. Ardeljan, R.J. McCabe, I.J. Beyerlein, M. Knezevic, Explicit incorporation of deformation twins into crystal plasticity finite element models, Computer Methods in Applied Mechanics and Engineering 295 (2015) 396–413.
[58] M. Knezevic, M.R. Daymond, I.J. Beyerlein, Modeling discrete twin lamellae in a microstructural framework, Scr. Mater. 121 (2016) 84–88.
[59] S.J. Owen, J.A. Brown, C.D. Ernst, H. Lim, K.N. Long, Hexahedral mesh generation for computational materials modeling, Procedia Engineering 203 (2017) 167–179.
[60] S.J. Owen, M.L. Staten, M.C. Sorensen, Parallel hex meshing from volume fractions, in: Proceedings of the 20th International Meshing Roundtable, Springer, 2011, pp. 161-178.
[61] Cubit, https://cubit.sandia.gov/, in.
[62] H. Lim, C.C. Battaile, J.E. Bishop, J.W. Foulk, Investigating mesh sensitivity and polycrystalline RVEs in crystal plasticity finite element simulations, Int. J. Plast. 121 (2019) 101–115.
[63] W.G. Feather, H. Lim, M. Knezevic, A numerical study into element type and mesh resolution for crystal plasticity finite element modeling of explicit grain structures, Comput. Mech. 67 (2021) 33–55.
[64] M. Knezevic, N.W. Landry, Procedures for reducing large datasets of crystal orientations using generalized spherical harmonics, Mechanics of Materials 88 (2015) 73–86.
[65] A. Eghtesad, T.J. Barrett, M. Knezevic, Compact reconstruction of orientation distributions using generalized spherical harmonics to advance large-scale crystal plasticity modeling: verification using cubic, hexagonal, and orthorhombic polycrystals, Acta. Mater. 155 (2018) 418–432.
[66] T.J. Barrett, A. Eghtesad, R.J. McCabe, B. Clausen, D.W. Brown, S.C. Vogel, M. Knezevic, A generalized spherical harmonics-based procedure for the interpolation of partial datasets of orientation distributions to enable crystal mechanics-based simulations, Materialia 6 (2019) 100328.
[67] B. Liu, D. Raabe, F. Roters, P. Eisenlohr, R.A. Lebensohn, Comparison of finite element and fast fourier transform crystal plasticity solvers for texture prediction, Modelling and Simulation in Materials Science and Engineering 18 (2010) 085005.
[68] E.H. Lee, Elastic-plastic deformation at finite strains, (1969).
[69] J.B. Shaffer, M. Knezevic, S.R. Kalidindi, Building texture evolution networks for deformation processing of polycrystalline fcc metals using spectral approaches: applications to process design for targeted performance, Int. J. Plast. 26 (2010) 1183–1194.
[70] S.R. Kalidindi, C.A. Bronkhorst, L. Anand, Crystallographic texture evolution in bulk deformation processing of FCC metals, J. Mech. Phys. Solids 40 (1992) 537–569.
[71] W.G. Feather, S. Ghorbanpour, D.J. Savage, M. Ardeljan, M. Jahedi, B. A. McWilliams, N. Gupta, C. Xiang, S.C. Vogel, M. Knezevic, Mechanical response, twinning, and texture evolution of WE43 magnesium-rare earth alloy as a function of strain rate: Experiments and multi-level crystal plasticity modeling, Int. J. Plast. 120 (2019) 180–204.
[72] R.J. Asaro, A. Needleman, Texture development and strain hardening in rate dependent polycrystals, Acta Metall. Mater. 33 (1985) 923–953.
[73] J.W. Hutchinson, Bounds and self-consistent estimates for creep of polycrystalline materials, Proceedings of the Royal Society of London. Series A, Mathematical and Physical Sciences, 348 (1976) 101-126.
[74] M. Zecevic, I.J. Beyerlein, R.J. McCabe, B.A. McWilliams, M. Knezevic, Transitioning rate sensitivities across multiple length scales: microstructure-property relationships in the Taylor cylinder impact test on zirconium, Int. J. Plast. 84 (2016) 138–159.
[75] W.G. Feather, D.J. Savage, M. Knezevic, A crystal plasticity finite element model embedding strain-rate sensitivities inherent to deformation mechanisms: application to alloy AZ31, Int. J. Plast. 143 (2021) 103031.
[76] J. Weiss, Y. Su, B.A. McWilliams, I.J. Beyerlein, M. Knezevic, Embedding strain-rate sensitivities of multiple deformation mechanisms to predict the behavior of a precipitate-hardened WE43 alloy under a wide range of strain rates, Mechanics of Materials 187 (2023) 104843.
[77] R.A. Lebensohn, A.K. Kanjarla, P. Eisenlohr, An elasto-viscoplastic formulation based on fast fourier transforms for the prediction of micromechanical fields in polycrystalline materials, International Journal of Plasticity 32 (2012) 59–69.
[78] M. Knezevic, M. Zecevic, I.J. Beyerlein, R.A. Lebensohn, A numerical procedure enabling accurate descriptions of strain rate-sensitive flow of polycrystals within crystal visco-plasticity theory, Computer Methods in Applied Mechanics and Engineering 308 (2016) 468–482.

[79] R. Bellman, G. Adomian, Green's functions for Partial differential equations, in: Partial Differential Equations, Springer, 1985, pp. 243–247.
[80] A.I. Zayed, A convolution and product theorem for the fractional fourier transform, IEEE Signal Processing Letters 5 (1998) 101–103.
[81] I.J. Beyerlein, C.N. Tomé, A dislocation-based constitutive law for pure zr including temperature effects, Int. J. Plast. 24 (2008) 867–895.
[82] R. Madec, B. Devincre, L. Kubin, T. Hoc, D. Rodney, The role of collinear interaction in dislocation-induced hardening, Science 301 (2003) 1879–1882.
[83] M. Knezevic, R.J. McCabe, C.N. Tomé, R.A. Lebensohn, S.R. Chen, C.M. Cady, G. T. Gray Iii, B. Mihaila, Modeling mechanical response and texture evolution of α-uranium as a function of strain rate and temperature using polycrystal plasticity, Int. J. Plast. 43 (2013) 70–84.
[84] M. Knezevic, I.J. Beyerlein, Multiscale modeling of microstructure-property relationships of polycrystalline metals during thermo-mechanical deformation, Advanced Engineering Materials 20 (2018) 1700956.
[85] H. Mecking, U.F. Kocks, Kinetics of flow and strain-hardening, Acta Metall. Mater. 29 (1981) 1865–1875.
[86] R. Madec, B. Devincre, L.P. Kubin, From dislocation junctions to Forest Hardening, Physical Review Letters 89 (2002) 255508.
[87] A. Eghtesad, M. Knezevic, High-performance full-field crystal plasticity with dislocation-based hardening and slip system back-stress laws: application to modeling deformation of dual-phase steels, J. Mech. Phys. Solids 134 (2020) 103750.
[88] M. Knezevic, I.J. Beyerlein, T. Nizolek, N.A. Mara, T.M. Pollock, Anomalous basal slip activity in zirconium under high-strain deformation, Mater. Res. Lett. 1 (2013) 133–140.
[89] F.F. Lavrentev, The type of dislocation interaction as the factor determining work hardening, Materials Science and Engineering 46 (1980) 191–208.
[90] U. Essmann, H. Mughrabi, Annihilation of dislocations during tensile and cyclic deformation and limits of dislocation densities, Philosophical Magazine A 40 (1979) 731–756.
[91] H. Mughrabi, A two-parameter description of heterogeneous dislocation distributions in deformed metal crystals, Materials Science and Engineering 85 (1987) 15–31.
[92] M. Knezevic, I.J. Beyerlein, D.W. Brown, T.A. Sisneros, C.N. Tomé, A polycrystal plasticity model for predicting mechanical response and texture evolution during strain-path changes: application to beryllium, Int. J. Plast. 49 (2013) 185–198.
[93] M. Zecevic, M. Knezevic, Modeling of sheet metal forming based on implicit embedding of the elasto-plastic self-consistent formulation in Shell elements: application to cup drawing of AA6022-T4, JOM 69 (2017) 922–929.
[94] M. Knezevic, L. Capolungo, C.N. Tomé, R.A. Lebensohn, D.J. Alexander, B. Mihaila, R.J. McCabe, Anisotropic stress-strain response and microstructure evolution of textured α-uranium, Acta. Mater. 60 (2012) 702–715.
[95] M. Knezevic, M. Jahedi, Y.P. Korkolis, I.J. Beyerlein, Material-based design of the extrusion of bimetallic tubes, Comput. Mater. Sci. 95 (2014) 63–73.
[96] M. Zecevic, M. Knezevic, A dislocation density based elasto-plastic self-consistent model for the prediction of cyclic deformation: application to Al6022-T4, Int. J. Plast. 72 (2015) 200–217.
[97] M. Zecevic, M. Knezevic, Latent hardening within the elasto-plastic self-consistent polycrystal homogenization to enable the prediction of anisotropy of AA6022-T4 sheets, Int. J. Plast. 105 (2018) 141–163.
[98] P. Version, MSC Software corporation, Newport Beach, CA, USA, 2013, p. 2013.
[99] Q. Liu, J. Li, J. Liu, ParaView visualization of abaqus output on the mechanical deformation of complex microstructures, Computers & Geosciences 99 (2017) 135–144.
[100] M. Ardeljan, I.J. Beyerlein, M. Knezevic, Effect of dislocation density-twin interactions on twin growth in AZ31 as revealed by explicit crystal plasticity finite element modeling, Int. J. Plast. 99 (2017) 81–101.
[101] M. Ardeljan, M. Knezevic, Explicit modeling of double twinning in AZ31 using crystal plasticity finite elements for predicting the mechanical fields for twin variant selection and fracture analyses, Acta. Mater. 157 (2018) 339–354.
[102] A. Prakash, R.A. Lebensohn, Simulation of micromechanical behavior of polycrystals: finite elements versus fast fourier transforms, Modelling and Simulation in Materials Science and Engineering 17 (2009) 064010.
[103] M. Zecevic, R.A. Lebensohn, L. Capolungo, New large-strain FFT-based formulation and its application to model strain localization in nano-metallic laminates and other strongly anisotropic crystalline materials, Mechanics of Materials 166 (2022) 104208.
[104] ABAQUS Version 6, Dassault Systèmes, Providence, RI, USA, (2017).
[105] C.K. Cocke, A.D. Rollett, R.A. Lebensohn, A.D. Spear, The AFRL additive Manufacturing modeling challenge: predicting micromechanical fields in AM IN625 using an FFT-based method with direct input from a 3D microstructural image, integrating materials and Manufacturing, Innovation 10 (2021) 157–176.
[106] Y. Xu, A non-local methodology for geometrically necessary dislocations and application to crack tips, Int. J. Plast. 140 (2021) 102970.
[107] J. Cheng, A. Shahba, S. Ghosh, Stabilized tetrahedral elements for crystal plasticity finite element analysis overcoming volumetric locking, Comput. Mech. 57 (2016) 733–753.
[108] A. Ma, F. Roters, D. Raabe, A dislocation density based constitutive model for crystal plasticity FEM including geometrically necessary dislocations, Acta. Mater. 54 (2006) 2169–2179.
[109] J. Jeong, G.Z. Voyiadjis, Crystal plasticity modeling for the strengthening effect of multilayered copper–graphene nanocomposites, J. Mech. Phys. Solids 181 (2023) 105468.